

Investigating the Circumnuclear Medium of Tidal Disruption Events with Radio Observations

CHANG ZHOU ¹, WEI-HUA LEI ¹, XIANGLI LEI ¹, PO MA ¹, SHAO-YU FU ^{1,2} AND ZI-PEI ZHU ^{1,2}

¹*Department of Astronomy, School of Physics, Huazhong University of Science and Technology, Wuhan, 430074, China*

²*Key Laboratory of Space Astronomy and Technology, National Astronomical Observatories, Chinese Academy of Sciences, Beijing, 100101, China*

ABSTRACT

Tidal disruption events (TDEs) are unique tools for investigating quiescent supermassive black hole (SMBH), accretion physics, and circumnuclear medium (CNM) environments. The CNM density profile is of great astrophysical significance, since it provides key diagnostics for the accretion history of dormant SMBH. TDEs can launch outflows that produce radio emission when propagating into the CNM. The closure relation (CR), i.e., the relation between the temporal indices and the spectral indices, are therefore monitoring the CNM density profile. In this work, we first collect 53 TDEs with radio observations to date. We then obtain the predicted CR for arbitrary CNM and different dynamical phases of the outflow, and apply to the radio TDE sample. We constrain the CNM density profile for 26 radio TDEs with good data quality. The results are generally consistent with those estimated with equipartition method, suggesting that CR analysis is efficient in the study of CNM profile for a quiescent SMBH.

Keywords: Tidal disruption (1696)

1. INTRODUCTION

Tidal disruption events (TDEs) occurs when a star passes too close to a SMBH and is torn apart by its intense tidal forces, producing luminous electromagnetic emission (Rees 1988; Phinney 1989). It has been observed in various wavelengths (radio, UV/optical, X-rays, even γ -ray in some jetted TDEs), providing useful tools to investigate quiescent SMBH, accretion physics and CNM environments.

The CNM density profile ($n \propto R^{-k}$) in quiescent galaxies reflects the accretion history of the central SMBH. Depending on the value of the density profile k , the corresponding physical scenarios are as follows: (1) $k = 1.5$, consistent with Bondi accretion (Bondi 1952); (2) $k \sim 2.5$, indicative of a past episode of super-Eddington accretion (Coughlin & Begelman 2014); and (3) $k \sim 1$, which may suggest replenishment by external stellar winds (Baganoff et al. 2003).

Theoretical and observational studies unveiled outflows (e.g., jet, wind, unbound tidal debris) in TDEs (Dai et al. 2018; Alexander et al. 2020; Dai et al. 2021; Qiao et al. 2025). Radio emissions are produced when the outflow interacts with the CNM. As the outflow expands, the radio emission observed at different epochs remains an indepen-

dent measurement of the CNM density profile at sub-parsec or even parsec scales, which are not directly resolvable at any wavelength with current facilities at the distance of most TDE hosts (Alexander et al. 2020).

Alexander et al. (2020) reviewed the radio observations of TDEs, focusing on nine TDEs with published radio detections. However, the sample of TDEs with radio detections has increased greatly recently (Cendes et al. 2024c; Goodwin et al. 2025a; Anumarlapudi et al. 2024). Some TDEs were previously characterized as non-detected, but have radio detections later on (Alexander et al. 2025). In this paper, we collect a sample of 53 TDEs with radio detections to date. A comprehensive study on the CNM environments of these radio TDEs are highly desired.

Equipartition analysis has been widely used to estimate the CNM profile of TDEs, which characterizes the system at minimum total energy (Barniol Duran et al. 2013). If the electron and magnetic field energies are close to equipartition then this lower limit is also a good estimate of their true energy. However, the outflow might contain additional components in the total energy (like that carried by protons), and the system would be far from the equipartition. Therefore, an independent method other than equipartition analysis, and a systematical investigation of the CNM profile for the full sample of radio TDEs are expected.

The synchrotron radio flux can be described by a series of power-law segments $F_\nu \propto \nu^{-\alpha} \nu^{-\beta}$ (Sari et al. 1998; Gao

et al. 2013; Zhang 2018). In such a model, the type of CNM can be tested with the closure relations (CRs, relations between the temporal indices α and spectral indices β), as did in gamma-ray bursts (GRBs) (Gao et al. 2013). Gao et al. (2013) only presented the CRs for constant-density ($k = 0$) and wind type ($k = 2$). In this work, to study the CNM type of radio TDEs, we obtain the results closure-relations for arbitrary CNM density profiles as described in several previous works (van Eerten & Wijers 2009; Fraija et al. 2021).

The structure of this paper is organized as follows. In Section 2, we collect the currently known sample of TDEs exhibiting radio emission. In Section 3, we provide the CR formulations corresponding to the interaction of an outflow with an arbitrary CNM density distribution in each dynamical phase, and provide the procedures for determining the spectral index and the temporal decay index. In Section 4, we report the results of CNM density profile index for a subset of the radio TDE sources with good data quality and discuss the implications of these results. The main conclusions are summarized in Section 5. A standard cosmology model is adopted with $H_0 = 67.3 \text{ km} \cdot \text{s}^{-1} \text{ Mpc}^{-1}$, $\Omega_M = 0.315$, $\Omega_\Lambda = 0.685$ (Planck Collaboration et al. 2014).

2. RADIO-DETECTED TDE SAMPLE

In this section, we collect a sample of radio-detected TDEs to date, including each event’s discovery date, redshift, and associated radio observations. Here, we provide a brief overview of their basic properties.

1. Sw J1644+57 was discovered on 2011 March 25 by the *Swift* satellite, which is consistent with an inactive galaxy at $z = 0.354$ (Bloom et al. 2011; Levan et al. 2011). It is the first TDE with a relativistic jet, which brings a helpful tool to investigate the dormant SMBH at a more distant position. The radio observation started on 2011 March 29.36, about 3.9 days after the first γ -ray detection. The radio light curve of Sw J1644+57 shows a re-brightening about 30 days after discovery (Berger et al. 2012; Zauderer et al. 2013), and it was well explained as a two-component jet model (Wang et al. 2014; Liu et al. 2015). The overall CNM density profile is $k_{\text{eq}} = 1.5$ derived from equipartition analysis (Eftekhari et al. 2018).
2. Swift J2058+05 was discovered by *Swift* on 2011 May 17–20 at a redshift of $z = 1.1853$. As the second jetted TDE after Swift J1644+57, it exhibits similar phenomenology (Cenko et al. 2012). The available radio data from Cenko et al. (2012) and Pasham et al. (2015) are insufficient to construct a broadband SED, and thus its CNM density profile cannot be constrained.
3. Swift J1112-82 was discovered by the *Swift* satellite in 2011 June 16-19, located in a galaxy with a redshift

of $z = 0.8901$ (Brown et al. 2015). It is the third TDE with a relativistic jet. The scarcity of radio observations makes it impossible to carry out a robust analysis (Brown et al. 2017).

4. AT2022cmc was discovered on 2020 February 11 by ZTF, which locate at a distant galaxy with $z = 1.19325$. It is the fourth on-axis jetted TDE, also the first jetted TDE discovered in optical (Andreoni et al. 2022; Pasham et al. 2023). The first radio emission was obtained about 5 days after its discovery (Andreoni et al. 2022; Pasham et al. 2023). Based on equipartition analysis and afterglow modeling, Matsumoto & Metzger (2023) roughly estimated the density profile of AT2022cmc is $k_{\text{eq}} \simeq 1.5 - 2$, and generally consistent with a Bondi-like accretion. In our previous work, we have constrained the CNM density profile with both CRs and detailed PyFRS¹ fit to the multi-band (optical, sub-millimeter, and radio) data of AT2022cmc, and we find $k_{\text{CR}} \simeq 1.47$ and $k_{\text{PyFRS}} \sim 1.68$ (Zhou et al. 2024).
5. EP250702a was first detected by Einstein Probe (EP) on 2025 July 2 at a redshift of $z = 1.036$ (Cheng et al. 2025; Li et al. 2025; Gompertz et al. 2026). Based on its multi-band properties, Li et al. (2025) proposed that EP250702a is highly likely to be a tidal disruption event of a white dwarf by an intermediate-mass black hole, and that it produced a relativistic jet. The first radio emission of EP250702a was detected by MeerKAT on 2025 July 4 (about 2.61 days after the EP trigger) (Bright et al. 2025).
6. Arp 299-B AT1 was initially discovered in the near-infrared (NIR), coincident with the western nucleus B1 of the nearby ($z = 0.010411$), luminous infrared galaxy Arp 299. Subsequent very long baseline interferometry (VLBI) radio observations resolved an expanding jet structure several years after the initial discovery (Mattila et al. 2018). However, the available radio data are limited, preventing the construction of a well-constrained spectral energy distribution (SED) for this source. Therefore, Arp 299-B AT1 is excluded from our analysis sample.
7. ASASSN-14ae was triggered by ASAS-SN on 2014 January 25, located at the nuclear of a galaxy at $z = 0.0436$ (Holoien et al. 2014). Cendes et al. (2024c) first detected ASASSN-14ae at 2313 days at 6GHz by VLA, and they also employed a late-time radio observation.

¹ <https://github.com/lelwh/PyFRS>

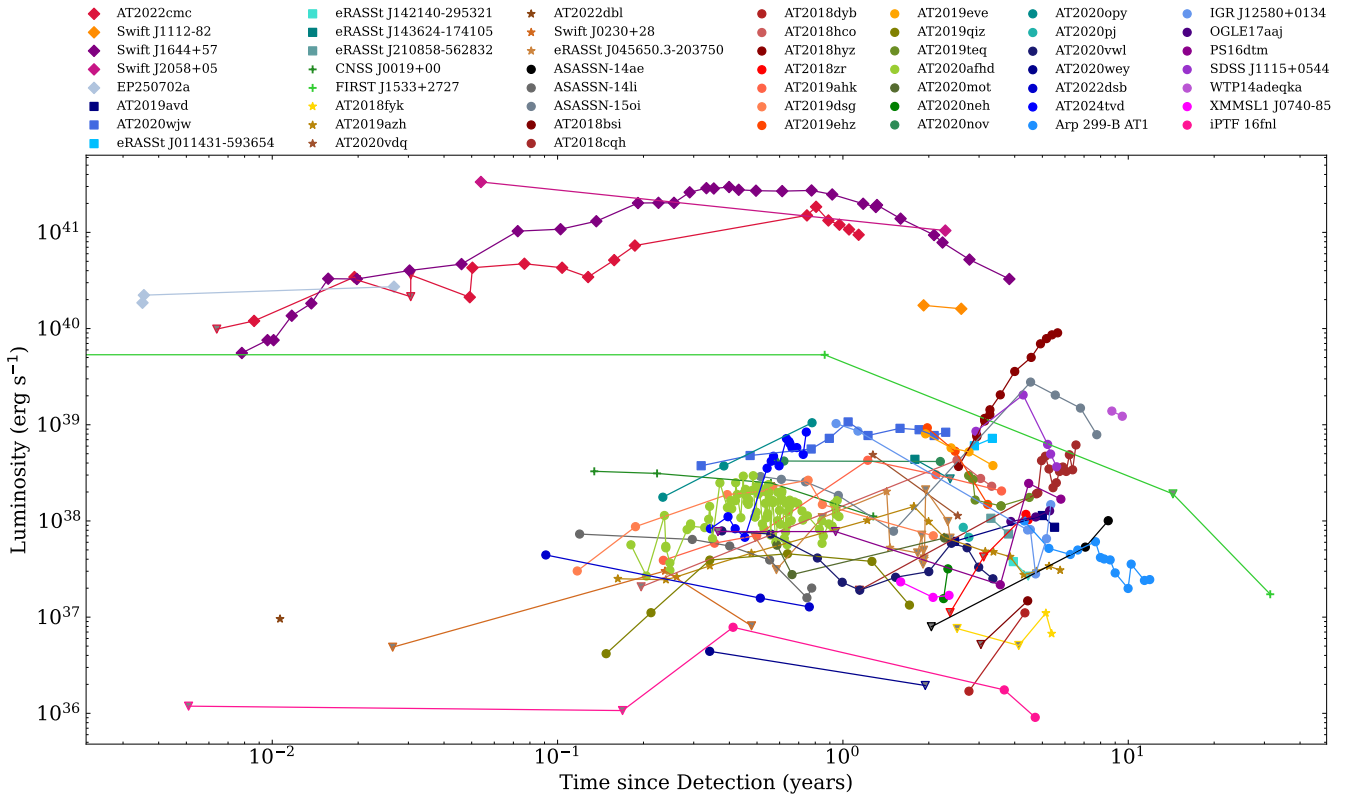


Figure 1. The radio light curves for our collected TDEs. To date, 53 TDEs have published radio detections. Although most of the detected TDEs were observed at multiple frequencies, for simplicity we show only a single frequency for each event. The triangles indicate the observations with published upper limits. The data can be available at <https://github.com/leiw/RadioTDEs>.

8. ASASSN-14li was optically discovered by the All Sky Automated Survey for SuperNovae (ASAS-SN) on 2014 November 22, it is consistent with a nearby galaxy ($z = 0.0206$) PGC 043234 (Jose et al. 2014). The initial radio data were obtained with the Arminute Microkelvin Imager Large Array (AMI-LA) on 2014-12-23.08, about a month after the first optical discovery (van Velzen et al. 2016). Since PGC 043234 had detected in radio before ASASSN-14li, probably due to a wake AGN, so we subtracted the radio emission from PGC 043234 like Alexander et al. (2016). Its radio emission also shows a standard synchrotron SED, the CNM profile from equipartition analysis is $k_{\text{eq}} = 2.5$ (Alexander et al. 2016).

9. ASASSN-15oi was discovered on 2015 August 14 at a redshift of $z = 0.0484$ in optical (Holoien et al. 2016). It also detected in X-ray, UV, and radio. Radio observation started on 2015 August 22, 8 days after the optical discovery, but without detections. Until 2016 February 12, a significant radio emission was detected (Horesh et al. 2021a), and long-time radio observations of ASASSN-15oi show two delayed radio flares at ~ 180 days and ~ 1400 days after optical discovery

(Hajela et al. 2025). Hajela et al. (2025) thought the first radio flare is due to stream-stream collisions.

10. AT2018bsi was optically discovered on 2018 April 9 at a distance of $z = 0.051$ (van Velzen et al. 2021). The radio emission was presented in Cendes et al. (2024c), however, the available data are too limited to enable a meaningful radio analysis.

11. AT2018cqh was first detected in a dwarf galaxy ($z = 0.048$) by Gaia on 16 June 2018, it was reported as a candidate TDE (Bykov et al. 2024). AT2018cqh has a delayed radio flare around 1105 days after the discovery time, the radio light curve shows an initial steep rise, flattening lasting about 544 days, and then follow another step rise (Zhang et al. 2024). The radio observations are not enough to show a detailed shape of the radio SED.

12. AT2018dyb/ASASSN-18pg was discovered on 11 July 2019 by ASAS-SN, located within a galaxy at $z = 0.018$ (Leloudas et al. 2019). About ~ 10 day after the optical discovery time, (Holoien et al. 2020) observed ASASSN-18pg by ATCA, and there were no signals detected. Recently, (Cendes et al. 2024c) sup-

plemented the radio data at late time. ASASSN-18pg has only one SED at 1615days, however, it is far from depicting its evolution.

13. AT2018fyk/ASASSN-18ul, with a redshift of 0.06, was first detected by ASAS-SN on 8 September 2018 (Stanek 2018). Its X-ray emission remained bright for ~ 500 days, dimmed around 600 days, and rebrightened near 1200 days, indicative of a partial TDE (Wevers et al. 2023). ATCA observations at 11, 38, 75 (Wevers et al. 2019) and at 225, 278, and 583 days (Wevers et al. 2021) yielded no-detections. However, recent MeerKAT L-band observations clearly detected the source, measuring 0.087 ± 0.013 mJy on 20 February 2024 and 0.0531 ± 0.0131 mJy on 15 May 2024 (Cendes et al. 2024a).
14. AT2018hco was discovered by ATLAS on 2018-10-04 at a redshift of $z = 0.088$, and it was first detected by ZTF on 2018-09-18 (van Velzen et al. 2021; Velzen et al. 2018). AT2018hco shows a delayed radio emission. There was no radio detection until ~ 1000 day (Horesh et al. 2018; Cendes et al. 2024c). Radio detections of AT2018hco offer 2 integral SEDs with the peak flux.
15. AT2018hyz/ASASSN-18zj was detected by ASAS-SN on 2018-11-06. It is consistent with a galaxy at $z = 0.04573$ (Hung et al. 2020; Short et al. 2020). AT2018hyz showed a delayed and bright radio flare relative to its optical detection. The CNM density profile consistent with $k_{\text{eq}} \sim 1$ (Cendes et al. 2022; Sfaradi et al. 2024).
16. AT2018zr/PS18kh was first discovered on 2 March 2018 by Pan-STARRS1. The flare is related to a galaxy at a redshift of $z = 0.071$ (Holoien et al. 2019a; Hung et al. 2019). The radio observations by AMI and VLA on 28 March 2018 and 30 March 2018, which yielded no detections (van Velzen et al. 2019b). The first radio detections was obtained at 1713days (Cendes et al. 2024c). Currently, there is only one SED for its radio data, it is challenging for us to search the CNM density profile of AT2018zr.
17. AT2019ahk/ASASSN-19bt was discovered on 2019 January 29.91 in the galaxy 2MASX J07001137-6602251, at a redshift of $z = 0.0262$. It is the first TDE flare detected by the Transiting Exoplanet Survey Satellite (TESS), and continued TESS observations show that the initial optical brighten happened on 2019 January 21.6 (Holoien et al. 2019b). Thus, we set the optical brighten time as the launch time of the outflow. The archival radio observations reveal a pre-disruption radio detection, which originates from the host galaxy. The initial radio detection related to ASASSN-19bt was obtained on 2019 March 3. We subtracted the host emission as described in Christy et al. (2024a). It shows unusual late-time radio evolution, as mentioned in Christy et al. (2024a), it might have a complex CNM environment.
18. AT2019azh was first discovered by ASAS-SN on 2019 February 22, with a redshift of $z = 0.022$ (Brimacombe et al. 2019). It was detected by ZTF on 2019 February 12 (van Velzen et al. 2019a). Long-time multiradio frequency observations of AT2019azh were presented by Goodwin et al. (2022), they derived an irregular density profile by equipartition. Combined with the 5.5GHz light curve and the predicted decay rates for a Sedov–Taylor solution, Goodwin et al. (2022) obtained the CNM profile of AT2019azh of $k = 2.5$. Sfaradi et al. (2022b) offered a more detailed light curve of 15.5GHz, which is well fitted by two components of synchrotron emitting sources. In our analysis, we set the first detected time of ZTF as the onset of the outflow.
19. AT2019dsg was discovered on 2019 April 09 as a nuclear transient at $z = 0.0512$ by ZTF (Nicholl et al. 2019). It was luminous in the X-ray, optical, UV and radio. On October 1, 2019, the IceCube Neutrino Observatory reported a neutrino detection $\sim 0.2\text{PeV}$, it is the first TDE related to neutrino (Stein et al. 2021). The initial radio emission of AT2019dsg was obtained on 2019 May 21. The CNM density profile was $k_{\text{eq}} = 1.7$ derived from equipartition analysis by using long-term radio observation (Cendes et al. 2021a).
20. AT2019ehz was discovered on 2019 April 29 at a redshift of $z = 0.074$ by Gaia (van Velzen et al. 2021). The first radio emission was detected on 2021 June 11, about 775 days after the Gaia detected time, it has two SEDs (970 days, 1262 days) well fitted by synchrotron emission. The CNM density profile of AT2019ehz derived from Cendes et al. (2024c) is $k_{\text{eq}} > 2.5$.
21. AT2019eve was discovered by ZTF on 2019 May 5 at $z = 0.0813$ (van Velzen et al. 2021). The radio detection started on 2021 June 11, about 769 days after the discovery time. It shows a late-time radio emission with three SEDs (945 days, 1102 days, 1325 days) consistent with synchrotron spectrum from a delayed outflow (Cendes et al. 2024c). The CNM density profile obtained from equipartition is steeper than 2.5 (Cendes et al. 2024c).
22. AT2019qiz is the most nearby TDE discovered to date. It was located at a redshift of $z = 0.01513$, corre-

- sponds to a distance of 65.6Mpc. It was discovered on 2019-09-19 by ZTF (Forster 2019), and the first detection was found from the Asteroid Terrestrial impact Last Alert System (ATLAS) on 2019-09-18 (Nicholl et al. 2020). O’Brien et al. (2019a,b) had reported the first radio detections of AT2019qiz by ATCA. Recently, Anumarlapudi et al. (2024) also given the lower-frequency observations of AT2019qiz. However, the radio data are still poor for us to employ an robust analysis.
23. AT2019teq was discovered in a galaxy at $z = 0.087$ on 2019 October 20 in optical observations (Hammerstein et al. 2023). An upper limit at radio frequencies was reported by VLASS at 351 days after the discovery. Later, Cendes et al. (2024c) presented VLA detections at 1096 day and 1155 day post-discovery.
 24. AT2020afhd was discovered by the Zwicky Transient Facility (ZTF) on 2020-10-20 at the nucleus of the galaxy LEDA 145386, with redshift of 0.027 (Arcavi et al. 2024). On 5 January 2024, an optical rebrightening was detected by ZTF (Fremling 2024), due to its blue continuum and bright UV flux, it was classified as a TDE (Hammerstein et al. 2024). The first radio emission was observed by VLA on 2024 February 9 UT 02:55 at 15.1GHz (Christy et al. 2024b). Wang et al. (2025) found AT2020afhd exhibit 19.6-day quasi-periodic variations in both X-ray and radio, and it was well explained by a disk-jet Lense-Thirring precession model. Thus, we can’t employ CR methods on the radio emission of AT2020afhd. We define the onset of the rebrightening to be MJD 60310, consistent with the choice made by Wang et al. (2025).
 25. AT2020mot was discovered in the optical band on 2020 June 14 at a redshift of $z = 0.070$ (Liodakis et al. 2023). Its 15-GHz observations by Liodakis et al. (2023) yielded only an upper limit of < 0.027 mJy, and a faint radio emission was detected from this source by Cendes et al. (2024c).
 26. AT2020neh was discovered on 19 June 2020 in optical by ZTF at a redshift of $z = 0.062$ (Angus et al. 2022). On 30 June 2020 and 31 December 2020, AT2020neh was observed twice at VLA but not detected. Recently, (Cendes et al. 2024c) reported only two detections at 874d and 905d in 6GHz. We cannot get enough information to constrain the CNM density profile through its poor radio observations.
 27. AT2020nov was discovered by ZTF on 2020 June 27, it located at a redshift of $z = 0.084$ (Frederick et al. 2020). The first radio emission data were reported by Cendes et al. (2024c), but the existing data are insufficient to construct a SED, preventing further analysis.
 28. AT2020opy was first detected on 2020 July 8 by ZTF at $z = 0.159$ (Gezari et al. 2020; Hammerstein et al. 2023). The radio emission of AT2020opy was initially obtained on 2020-10-6, about 90 day after the ZTF detection. The CNM density profile around the SMBH obtained by equipartition is $k_{\text{eq}} \sim 1.5 - 2.5$, and the linear increase of the outflow energy means that there is a constant energy injected into the outflow (Goodwin et al. 2023a).
 29. AT2020pj was discovered by ZTF on 2020 January 2 at a redshift of $z = 0.068$. The first radio emission data were reported by Cendes et al. (2024c); however, the existing data are insufficient to construct an SED, precluding further analysis.
 30. AT2020vwl was first detected on 2020 October by ZTF, located in a galaxy with a redshift of $z = 0.0325$ (Yao et al. 2023). The first radio emission detected on 2021 February 23. Its long-time light curve reveal two radio flares(Goodwin et al. 2023b, 2025b). Although there was no previous significant AGN activity, there could be low-level host radio emission from low-luminosity AGN or star formation, so we subtracted host radio emission like Goodwin et al. (2023b). Goodwin et al. (2025b) thought the second radio flare was due to an energy injection into the pre-existing outflow or a second new outflow.
 31. AT2020wey was discovered on 2020 October 8 by ZTF, and was classified as a TDE in a post-starburst galaxy at a redshift of $z = 0.027$ (Nordin et al. 2020a; Arcavi et al. 2020). The radio emission, detected 128 days post-discovery (Cendes et al. 2024c), represents the only available radio data to date. However, this single epoch precludes a more detailed analysis.
 32. AT2022dbl/ASASSN-22ci is a nearby TDE discovered by ASAS-SN on 22 February 2022, with a redshift of 0.0284 (Stanek 2022; Arcavi et al. 2022). Its optical emission faded to the host-galaxy level within roughly a year of peak, but nearly two years after the initial outburst, ZTF detected a second brightening (Yao et al. 2024), the similarity between the two flares suggests that AT2022dbl is a multiple/repeating partial TDE (Hinkle et al. 2024). A faint radio signal of 32 ± 7 mJy at 15 GHz was detected with the VLA on 2022 February 26 (Sfaradi et al. 2022a) and no further radio activity has been reported to date.
 33. AT2022dsb/eRASS154221.6-224012 was discovered by the extended ROentgen Survey with an Imag-

- ing Telescope Array (eROSITA; [Predehl et al. \(2021\)](#)) on 2022 February 17, consistent with the galaxy ESO 583-G004 at a redshift of $z = 0.0235$. AT2022dsb was observed by the Australia Telescope Compact Array (ATCA) three times, only six radio data was obtained ([Malyali et al. 2024](#)).
34. AT2024tvd was discovered by ZTF on 25 August 2024 at a redshift of 0.044938, located 1.24 ± 0.30 arcsec from the host-galaxy nucleus, identifying it as an offset TDE ([Sollerman et al. 2024](#); [Yao et al. 2025](#)). [Faris et al. \(2024\)](#) classified it as a TDE based on broad H and He II in the spectrum, central location in its host galaxy, and persistent UV emission. A radio counterpart was detected with VLA on 3 January 2025 (~ 131 days after discovery), yielding a 10 GHz flux of 0.60 ± 0.06 mJy ([Sfaradi et al. 2025a](#)). AMI subsequently measured 0.72 ± 0.07 mJy at 15.5 GHz on 13 January 2025 ([Horesh et al. 2025](#)). Long-term monitoring shows that its radio emission exhibits a double-peaked evolution ([Sfaradi et al. 2025b](#)).
 35. CNSS J0019+00 was identified in the Caltech–NRAO Stripe 82 Survey (CNSS) on 2015 March 21, it located in a nearby galaxy whose redshift is 0.018 ([Anderson et al. 2020](#)). It is the first radio-discovered TDE, so we cannot set its discovery time as the onset of the outflow. It has no significant X-ray or optical emission. The radio spectra are well fit by a synchrotron spectrum, and the CNM profile of CNSS J0019+00 obtained from equipartition analysis is $k_{\text{eq}} = 2.5$ ([Anderson et al. 2020](#)).
 36. AT2019avd was first detected by ZTF on 9 February 2019, located at the nuclear of a quiescent galaxy at a redshift of $z = 0.029$ ([Malyali et al. 2021](#)). It was also detected in radio, IR, UV, and X-ray wavelengths. [Wang et al. \(2023\)](#) report the radio emission of AT2019avd from VLA and VLBA.
 37. AT2020wjw/eRASSt J234402.9-352640 was first discovered on 2020 November 28 by the eROSITA instrument, it coincides with the nuclear of the galaxy WISEA J234402.95-352641.8 at $z = 0.1$ ([Homan et al. 2023](#)). The first radio emission was detected by [Goodwin et al. \(2024\)](#) on 2021 April 5 with ATCA, and they inferred the CNM density profile of J2344 is $k_{\text{eq}} = 1.4$ from equipartition modelling of the spectral properties. J2344 was detected in multiband that includes X-ray, UV, optical, infrared, and radio. The early X-ray and optical emission suggest J2344 likely a TDE in a turned-off AGN ([Homan et al. 2023](#)), therefore, we subtracted the radio emission from its host like [Goodwin et al. \(2024\)](#) before our analysis.
 38. eRASSt J011431–593654 ($z = 0.16$) exhibited an X-ray flux peak detected by eROSITA on 2020 November 24. As reported in [Goodwin et al. \(2025a\)](#), this source was subsequently observed with the Australia Telescope Compact Array (ATCA) during two epochs separated by six months, with radio emission detected 1224 days after the X-ray peak.
 39. eRASSt J142140-295321 ($z = 0.056$) exhibited an X-ray flux peak detected by eROSITA on 2020 January 30. As reported in [Goodwin et al. \(2025a\)](#), this source was subsequently observed with ATCA during two epochs separated by six months, with radio emission detected 1526 days after the X-ray peak.
 40. eRASSt J143624-174105 ($z = 0.19$) exhibited an X-ray flux peak detected by eROSITA on 2022 February 18. As reported in [Goodwin et al. \(2025a\)](#), this source was subsequently observed with ATCA during two epochs separated by six months, with radio emission detected 777 days after the X-ray peak.
 41. eRASSt J210858-562832 $z = 0.043$ exhibited an X-ray flux peak detected by eROSITA on 2020 October 26. As reported in [Goodwin et al. \(2025a\)](#), this source was subsequently observed with ATCA during two epochs separated by six months. Through analysis of archival radio observations, they found a radio emission from the Australian Square Kilometre Array Pathfinder (ASKAP) Rapid ASKAP Continuum Survey (RACS) at 70.7 days after the X-ray peak.
 42. FIRST J1533+2727 is the second TDE discovered in radio. It was first detected by the Green Bank 300 foot telescope in 1986 and 1987 at $z = 0.03243$. Interestingly, FIRST J1533+2727 was faded by a factor of 400 over 33 year at 5.5 GHz ([Ravi et al. 2022](#)). Unfortunately, the radio data are not good enough to obtain the CNM density profile with our CR analysis.
 43. IGR J12580+0134 was discovered by INTEGRAL as the tidal disruption of a super-Jupiter by a SMBH on 2011 January 2-11, associated to a nearby galaxy NGC 4845, at a redshift of $z = 0.00411$ ([Nikołajuk & Walter 2013](#)). The early time emission at 100 to 857GHz based on Planck all-sky survey was shown in [Yuan et al. \(2016\)](#), radio emission from IGR J12580+0134 has also been detected by JVLA at 1.57 and 6 GHz about one year after the X-ray peak ([Irwin et al. 2015](#)), and late-time radio emission detected by VLA and VLBA was given by [Perlman et al. \(2017\)](#). IGR J12580+0134 is the first TDE with an off-axis relativistic jet ([Lei et al. 2016](#); [Yuan et al. 2016](#)).

44. iPTF 16fnl was discovered on 2016-08-26 by the intermediate Palomar Transient Factory (iPTF) survey at $z = 0.016328$ (Gezari et al. 2016). iPTF 16fnl was detected in radio in the third epoch of the VLA observation at ~ 153 day after the optical discovery, and showed a delayed radio flare (Horesh et al. 2021b; Cendes et al. 2024c).
45. OGLE17aaj was optically discovered by the 8.2 m Antu telescope of the Very Large Telescope (VLT) on 2017 January 2, it occurred in the nucleus of a weakly active galaxy at a redshift of $z = 0.116$ (Gromadzki et al. 2019). The first radio emission was detected at 1581 days after discovery (Cendes et al. 2024c).
46. PS16dtm/SN2016ezh was discovered at redshift of $z = 0.0804$ on 12 August 2016 by Pan-STARRS1 (Blanchard et al. 2017; Jiang et al. 2017; Petrushevska et al. 2023). It is a TDE happened in a pre-existing AGN.
47. SDSS J111536.57+054449.7 (hereafter SDSS J1115+0544) was initially identified through a systematic search for mid-infrared (MIR) outbursts in nearby galaxies (Jiang et al. 2021), it was located at a redshift of $z = 0.08995$. The time of the optical peak is 2015.5.28 (MJD 57170). It was also detected in UV, optical and radio (Yan et al. 2019; Zhang et al. 2026). It showed a delayed radio emission relative to the optical peak time. There are too few data to fully describe their SEDs, thus, we cannot ensure the reliability of our results.
48. Swift J023017.0+283603 was observed with Swift/XRT from December 2021 to January 2022 with no X-ray detection. Chen et al. (2021) subsequently reported a supernova, SN2021afkk, located $4'$ away. However, an X-ray source was later detected by *Swift* on 22 June 2022 with a redshift of 0.036, given its soft spectrum and proximity to a galaxy, it was identified as the TDE candidate Swift J0230+28 (Evans et al. 2022). Long-term monitoring revealed recurrent soft X-ray flares with a period of ~ 22 days (Guolo et al. 2024). VLA observations detected a radio counterpart: nondetections on 2 July and 20 December 2022 yielded upper limits of 0.015 mJy and 0.025 mJy, while a flux of 0.093 ± 0.007 mJy was measured on 20 September 2022. The radio nondetections coincide with X-ray quiescent phases, whereas the detection aligns with an X-ray active phase (Guolo et al. 2024). Given the very limited radio coverage, we are unable to perform a meaningful CR analysis for this source.
49. WTP14adeqka was first detected by WISE on 20 June 2015, located at the redshift of 0.01895. Its mid-infrared (MIR) light curve exhibits high luminosity, peaking at $10^{43} \text{ erg s}^{-1}$ approximately, while showing no counterpart in optical or X-ray bands (Masterson et al. 2024). Golay et al. (2025) conducted a detailed radio study of WTP14adeqka at 4 – 10 years post-disruption, thereby establishing it as the first mid-infrared TDE with detected delayed radio emission. We set the disruption time to 2015 April 19, following the IR light-curve modeling of Masterson et al. (2024).
50. XMMSL1 J074008.2-853927 (hereafter XMMSL1 J0740-85) was detected from a galaxy at a redshift of $z = 0.0173$ by the XMM-Newton slew survey on 2014 April 1. It included both thermal and non-thermal emissions (Saxton et al. 2017). The ATCA observation of XMMSL1 J0740-85 started on 2015 November 14, 592d after the X-ray discovery (Alexander et al. 2017). The CNM density profile of XMMSL1 J0740-85 is $k_{\text{eq}} \sim 1$ inferred from equipartition analysis (Alexander et al. 2017).
51. eRASSt J045650.3-203750 is a nuclear transient discovered in the eRASS2 all-sky survey between 2020 September 8 and 10, located in the nucleus of a quiescent galaxy at a redshift of $z = 0.077$ (Liu et al. 2023). Long-term X-ray and ultraviolet monitoring reveals recurrent outbursts with a characteristic recurrence timescale of approximately 223 days, indicating that the source is a repeating nuclear transient. Transient radio emission is also detected in eRASSt J045650.3-203750 (Liu et al. 2024).
52. AT2019aalc was discovered by ZTF on January 22, 2019, and is located in a galaxy at redshift $z = 0.0356$. It exhibits multi-wavelength emission spanning radio, infrared, optical, ultraviolet, X-ray, and neutrino radiation. Milán Veres et al. (2024) conducted multi-wavelength monitoring from radio to X-rays and identified two distinct optical flares. During the second optical flare, a notably bright UV counterpart and multiple X-ray flares were observed, accompanied by IR dust echo emission. According to the large-amplitude variability detected by VLASS, along with the high brightness temperature ($T_b \gg 10^5$ K) measured by EVN at 1.7 GHz, Therefore, AT2019aalc is interpreted as a TDE occurring within an AGN. Unfortunately, Milán Veres et al. (2024) does not report any results from the radio data analysis.
53. AT2020vdq was first detected by ZTF on 4 October 2020, with a redshift of $z = 0.045$ (Nordin et al. 2020b). Nearly 1000 days after the initial outburst, a new optical flare was detected near its position (Charalampopoulos et al. 2023), suggesting that AT2020vdq

is a repeating partial TDE. Somalwar et al. (2025) reported that on 9 October 2021 approximately 383 days after the optical peak, VLASS detected a 3 GHz radio flux of 1.48 ± 0.14 mJy. Their multiwavelength analysis, including modeling of the radio emission, showed that the source can be described by a non-relativistic spherical synchrotron model.

The information of these TDEs are summarized in Table A1, and the radio light curves (around 5 GHz) for these TDEs are plotted in Figure 1, except AT2019aal, because its radio data are not published.

3. CONSTRAINING THE CNM PROFILE WITH CR ANALYSIS

The radio afterglow of TDEs can be interpreted as synchrotron emission originating from the forward shock (FS) driven by the interaction between the jet/outflow and the CNM. Its flux density is typically characterized by a series of power-law segments, $F_\nu \propto t^{-\alpha} \nu^{-\beta}$ (Sari et al. 1998; Gao et al. 2013; Zhang 2018). Within this framework, the type of CNM can be constrained using the CRs, following the same principle as is commonly applied in gamma-ray burst (GRB) studies. (Gao et al. 2013). We generalize the CRs derived by Gao et al. (2013) for a constant density ($k = 0$) and a wind type density profile ($k = 2$) to the case of an arbitrary density profile as described in several previous works (van Eerten & Wijers 2009; Fraija et al. 2021).

Generally, the jet evolution can be characterized by four phases. The first is a coasting phase, during which the Lorentz factor remains approximately constant, $\Gamma(t) \simeq \Gamma_0$. In the second phase, the shell starts to decelerate when the mass m of the CNM swept by the FS is about $1/\Gamma_0$ of the rest mass in the ejecta M_{ej} . The shell then approaches the Blandford & McKee (1976) self-similar evolution. Subsequently, the ejecta enters the post-jet-break phase once the beaming angle $1/\Gamma$ becomes larger than the jet half-opening angle θ_j . Eventually, the blastwave transitions to the Newtonian deceleration phase after sweeping up CNM with a total rest-mass energy comparable to the initial energy of the ejecta, and the dynamics is governed by the well-known Sedov-Taylor solution.

We consider a relativistic thin shell or a non-relativistic outflow expanding into the pre-existing CNM with density (Rees & Meszaros 1992; Mészáros & Rees 1997; Sari et al. 1998; Zhang 2018; Huang & Liu 2021),

$$n(R) = n_{18} \left(\frac{R}{10^{18} \text{cm}} \right)^{-k} = AR^{-k}, \quad (1)$$

where n_{18} is the CNM density at $R = 10^{18}$ cm. During the interaction of jet/outflow and the CNM, electrons are accelerated at the shock front to a power-law distribution $N(\gamma_e) \propto$

γ_e^{-p} . Under the assumption that two fractions ϵ_e and ϵ_B of the shock energy $e_2 = 4\Gamma^2 n m_p c^2$ is deposited into electrons and magnetic field, respectively. This defines the minimum injected electron Lorentz factor (Zhang 2018; Sari et al. 1998),

$$\gamma_m = \frac{p-2}{p-1} \epsilon_e (\Gamma-1) \frac{m_p}{m_e}, \quad (2)$$

and the comoving magnetic field

$$B = (32\pi m_p \epsilon_B n)^{1/2} c. \quad (3)$$

where m_e and m_p are electron mass and proton mass. The synchrotron power and characteristic frequency emitted by an electron with Lorentz factor γ_e are given by (Rybicki & Lightman 1979)

$$P(\gamma_e) \simeq \frac{4}{3} \sigma_T c \Gamma^2 \gamma_e^2 \frac{B^2}{8\pi}, \quad (4)$$

$$\nu(\gamma_e) \simeq \Gamma \gamma_e^2 \frac{q_e B}{2\pi m_e c (1+z)}, \quad (5)$$

where σ_T is the Thomson cross-section, q_e is electron charge. The peak of the spectra power occurs at $\nu(\gamma_e)$, and (Sari et al. 1998; Gao et al. 2013; Zhang 2018)

$$P_{\nu, \text{max}} \simeq \frac{P(\gamma_e)}{\nu(\gamma_e)(1+z)} = \frac{m_e c^2 \sigma_T}{3q_e} \Gamma B. \quad (6)$$

The critical electron Lorentz factor γ_c is defined by equating the electron's synchrotron cooling timescale to the observer-frame time t (Rybicki & Lightman 1979; Sari et al. 1998),

$$\gamma_c = \frac{6\pi m_e c}{\Gamma \sigma_T B^2 t / (1+z)}, \quad (7)$$

Radiative cooling and continuous injection of accelerated electrons shape the electron distribution into a broken power law. The resulting synchrotron spectrum is then divided by three characteristic frequencies into multiple power-law segments (Gao et al. 2013; Zhang 2018). The first two characteristic frequencies ν_m and ν_c are determined by the two electron Lorentz factors γ_m and γ_c , respectively. The third characteristic frequency is the self-absorption frequency ν_a , below which the synchrotron photons are self-absorbed. This frequency can be derived from both the optical depth method (i.e., where the optical depth for photon self-absorption is unity) and the blackbody method (i.e., where the synchrotron flux equals the blackbody radiation flux) (Gao et al. 2013; Zhang 2018; Shen & Zhang 2009). The maximum flux density is given by $F_{\nu, \text{max}} = (1+z) N_e P_{\nu, \text{max}} / 4\pi D^2$ (Sari et al. 1998), where $N_e = \int 4\pi R^2 n dR$ is the total number of electrons in shocked CNM and D is the distance of the source.

3.1. Closure relations (CRs)

3.1.1. Relativistic Jet in Coasting Phase

The relativistic jet first undergoes a coasting phase, in which the dynamic evolution is given by

$$\begin{aligned}\Gamma &\simeq \Gamma_0, \\ R(t) &\simeq 2c\Gamma_0^2 t.\end{aligned}\quad (8)$$

We can then derive the scalings for FS spectra parameters in this phase as

$$v_m \propto t^{-k/2}, \quad v_c \propto t^{\frac{3k-4}{2}}, \quad F_{V,\max} \propto t^{\frac{6-3k}{2}}. \quad (9)$$

For $v_a < v_c < v_m$, we have $v_a \propto t^{\frac{8-9k}{5}}$ and,

$$F_V = F_{V,\max} \times \begin{cases} \left(\frac{v_a}{v_c}\right)^{\frac{1}{3}} \left(\frac{v}{v_a}\right)^2 \propto t^{1+k} v^2, & v < v_a \\ \left(\frac{v}{v_c}\right)^{\frac{1}{3}} \propto t^{\frac{11-6k}{3}} v^{\frac{1}{3}}, & v_a < v < v_c \\ \left(\frac{v}{v_c}\right)^{-\frac{1}{2}} \propto t^{\frac{8-3k}{4}} v^{-\frac{1}{2}}, & v_c < v < v_m \\ \left(\frac{v_m}{v_c}\right)^{-\frac{1}{2}} \left(\frac{v}{v_m}\right)^{-\frac{p}{2}} \propto t^{\frac{8-2k-kp}{4}} v^{-\frac{p}{2}}, & v_m < v \end{cases} \quad (10)$$

For $v_a < v_m < v_c$, we have $v_a \propto t^{\frac{3-4k}{5}}$ and,

$$F_V = F_{V,\max} \times \begin{cases} \left(\frac{v_a}{v_m}\right)^{\frac{1}{3}} \left(\frac{v}{v_a}\right)^2 \propto t^2 v^2, & v < v_a \\ \left(\frac{v}{v_m}\right)^{\frac{1}{3}} \propto t^{\frac{9-4k}{3}} v^{\frac{1}{3}}, & v_a < v < v_m \\ \left(\frac{v}{v_m}\right)^{-\frac{p-1}{2}} \propto t^{\frac{12-5k-kp}{4}} v^{-\frac{p-1}{2}}, & v_m < v < v_c \\ \left(\frac{v_c}{v_m}\right)^{-\frac{p-1}{2}} \left(\frac{v}{v_c}\right)^{-\frac{p}{2}} \propto t^{\frac{8-2k-kp}{4}} v^{-\frac{p}{2}}, & v_c < v \end{cases} \quad (11)$$

For $v_m < v_a < v_c$, we have $v_a \propto t^{\frac{4-6k-kp}{2(p+4)}}$ and,

$$F_V = F_{V,\max} \times \begin{cases} \left(\frac{v_m}{v_a}\right)^{\frac{p+4}{2}} \left(\frac{v}{v_m}\right)^2 \propto t^2 v^2, & v < v_m \\ \left(\frac{v_a}{v_m}\right)^{-\frac{p-1}{2}} \left(\frac{v}{v_a}\right)^{\frac{5}{2}} \propto t^{\frac{8+k}{4}} v^{\frac{5}{2}}, & v_m < v < v_a \\ \left(\frac{v}{v_m}\right)^{-\frac{p-1}{2}} \propto t^{\frac{12-5k-kp}{4}} v^{-\frac{p-1}{2}}, & v_a < v < v_c \\ \left(\frac{v_c}{v_m}\right)^{-\frac{p-1}{2}} \left(\frac{v}{v_c}\right)^{-\frac{p}{2}} \propto t^{\frac{8-2k-kp}{4}} v^{-\frac{p}{2}}, & v_c < v \end{cases} \quad (12)$$

3.1.2. Relativistic Jet in Deceleration Phase

For a relativistic jet, it will approach the [Blandford & McKee \(1976\)](#) self-similar evolution when it is decelerated. The dynamic evolution of the blastwave for arbitrary k density profile is given by

$$\begin{aligned}\Gamma(t) &\simeq \left(\frac{(17-4k)E_{K,\text{iso}}}{4^{5-k}(4-k)^{3-k}\pi A m_p c^5 t^{3-k}} \right)^{\frac{1}{2(4-k)}}, \\ R(t) &\simeq \left(\frac{(17-4k)(4-k)E_{K,\text{iso}} t}{4\pi A m_p c} \right)^{\frac{1}{(4-k)}},\end{aligned}\quad (13)$$

where m_p is proton mass. From Equation (13), $\Gamma \propto t^{-\frac{(3-k)}{2(4-k)}}$ and $R \propto t^{\frac{1}{4-k}}$, one has the scalings for the FS spectra parameters in this phase as

$$v_m \propto t^{-3/2}, \quad v_c \propto t^{\frac{4-3k}{2(k-4)}}, \quad F_{V,\max} \propto t^{\frac{k}{2(k-4)}}. \quad (14)$$

For $v_a < v_c < v_m$, we have $v_a \propto t^{\frac{3k+10}{5(k-4)}}$ and,

$$F_V = F_{V,\max} \times \begin{cases} \left(\frac{v_a}{v_c}\right)^{\frac{1}{3}} \left(\frac{v}{v_a}\right)^2 \propto t^{\frac{4}{4-k}} v^2, & v < v_a \\ \left(\frac{v}{v_c}\right)^{\frac{1}{3}} \propto t^{\frac{3k-2}{3(k-4)}} v^{\frac{1}{3}}, & v_a < v < v_c \\ \left(\frac{v}{v_c}\right)^{-\frac{1}{2}} \propto t^{-\frac{1}{4}} v^{-\frac{1}{2}}, & v_c < v < v_m \\ \left(\frac{v_m}{v_c}\right)^{-\frac{1}{2}} \left(\frac{v}{v_m}\right)^{-\frac{p}{2}} \propto t^{\frac{2-3p}{4}} v^{-\frac{p}{2}}, & v_m < v \end{cases} \quad (15)$$

For $v_a < v_m < v_c$, we have $v_a \propto t^{-\frac{3k}{5(4-k)}}$ and,

$$F_V = F_{V,\max} \times \begin{cases} \left(\frac{v_a}{v_m}\right)^{\frac{1}{3}} \left(\frac{v}{v_a}\right)^2 \propto t^{\frac{2}{4-k}} v^2, & v < v_a \\ \left(\frac{v}{v_m}\right)^{\frac{1}{3}} \propto t^{\frac{2-k}{4-k}} v^{\frac{1}{3}}, & v_a < v < v_m \\ \left(\frac{v}{v_m}\right)^{-\frac{p-1}{2}} \propto t^{-\frac{12p-12+5k-3kp}{16-4k}} v^{-\frac{p-1}{2}}, & v_m < v < v_c \\ \left(\frac{v_c}{v_m}\right)^{-\frac{p-1}{2}} \left(\frac{v}{v_c}\right)^{-\frac{p}{2}} \propto t^{-\frac{3p-2}{4}} v^{-\frac{p}{2}}, & v_c < v \end{cases} \quad (16)$$

For $v_m < v_a < v_c$, we have $v_a \propto t^{\frac{2k-3kp+8+12p}{2(p+4)(k-4)}}$ and,

$$F_V = F_{V,\max} \times \begin{cases} \left(\frac{v_m}{v_a}\right)^{\frac{p+4}{2}} \left(\frac{v}{v_m}\right)^2 \propto t^{\frac{2}{4-k}} v^2, & v < v_m \\ \left(\frac{v_a}{v_m}\right)^{-\frac{p-1}{2}} \left(\frac{v}{v_a}\right)^{\frac{5}{2}} \propto t^{\frac{20-3k}{4(4-k)}} v^{\frac{5}{2}}, & v_m < v < v_a \\ \left(\frac{v}{v_m}\right)^{-\frac{p-1}{2}} \propto t^{\frac{12+3kp-5k-12p}{4(4-k)}} v^{-\frac{p-1}{2}}, & v_a < v < v_c \\ \left(\frac{v_c}{v_m}\right)^{-\frac{p-1}{2}} \left(\frac{v}{v_c}\right)^{-\frac{p}{2}} \propto t^{\frac{2-3p}{4}} v^{-\frac{p}{2}}, & v_c < v \end{cases} \quad (17)$$

The results are consistent with the results of [van Eerten & Wijers \(2009\)](#), see Tables 1 and 2 therein), but they do not include the self-absorption frequency v_a .

3.1.3. Non-relativistic Outflow in Coasting phase

For a non-relativistic outflow, the magnetic field is given by

$$B = (4\pi m_p \epsilon_B n)^{1/2} v, \quad (18)$$

where v is the velocity of the blastwave. The minimum electron Lorentz factor is

$$\gamma_m = \epsilon_e \frac{p-2}{p-1} \frac{m_p}{m_e} \frac{v^2}{c^2}. \quad (19)$$

When the outflow under coasting phase, the dynamic evolution can be described by

$$\begin{aligned}v &\simeq v_0, \\ R(t) &\simeq vt.\end{aligned}\quad (20)$$

From Equation (20), $R \propto t$ and v are independent to time, one has the scalings for the FS spectra parameters in this phase as $v_m \propto t^{-k/2}$, $v_c \propto t^{\frac{3k-4}{2}}$, and $F_{V,\max} \propto t^{\frac{6-3k}{2}}$, similar to the case of a relativistic jet in coasting phase. Thus, whether it is a relativistic outflow or a non-relativistic outflow, their CRs during the coasting phase are the same.

3.1.4. Non-relativistic Outflow in Deceleration phase

If the outflow is Newtonian, the dynamic evolution can be described by the Sedov-Taylor (ST) solution in deceleration phase,

$$R(t) \simeq \left(\frac{5-k}{2}\right)^{\frac{2}{5-k}} \left[\frac{(3-k)E_{k,\text{iso}}}{2\pi A m_p}\right]^{\frac{1}{5-k}} t^{\frac{2}{5-k}}, \quad (21)$$

$$v(t) \simeq \left(\frac{5-k}{2}\right)^{\frac{k-3}{5-k}} \left[\frac{(3-k)E_{k,\text{iso}}}{2\pi A m_p}\right]^{\frac{1}{5-k}} t^{\frac{k-3}{5-k}}.$$

From Equation (21), $R \propto t^{\frac{1}{5-k}}$ and $v \propto t^{\frac{k-3}{5-k}}$, one has the scalings for the FS spectra parameters in this phase as

$$v_m \propto t^{\frac{4k-15}{5-k}}, \quad v_c \propto t^{\frac{2k-1}{5-k}}, \quad F_{V,\max} \propto t^{\frac{3-2k}{5-k}}. \quad (22)$$

For $v_a < v_m < v_c$, we have $v_a \propto t^{\frac{30-16k}{5(5-k)}}$ and,

$$F_V = F_{V,\max} \times \begin{cases} \left(\frac{v_a}{v_m}\right)^{\frac{1}{3}} \left(\frac{v}{v_a}\right)^2 \propto t^{\frac{2(k-1)}{5-k}} v^2, & v < v_a \\ \left(\frac{v}{v_m}\right)^{\frac{1}{3}} \propto t^{\frac{24-10k}{3(5-k)}} v^{\frac{1}{3}}, & v_a < v < v_m \\ \left(\frac{v}{v_m}\right)^{-\frac{p-1}{2}} \propto t^{\frac{21-8k+4kp-15p}{2(5-k)}} v^{-\frac{p-1}{2}}, & v_m < v < v_c \\ \left(\frac{v_c}{v_m}\right)^{-\frac{p-1}{2}} \left(\frac{v}{v_c}\right)^{-\frac{p}{2}} \propto t^{\frac{20-6k+4kp-15p}{2(5-k)}} v^{-\frac{p}{2}}, & v > v_c \end{cases} \quad (23)$$

For $v_m < v_a < v_c$, we have $v_a \propto t^{\frac{10-8k+4kp-15p}{(5-k)(p+4)}}$ and,

$$F_V = F_{V,\max} \times \begin{cases} \left(\frac{v_m}{v_a}\right)^{\frac{p+4}{2}} \left(\frac{v}{v_m}\right)^2 \propto t^{\frac{2(k-1)}{5-k}} v^2, & v < v_m \\ \left(\frac{v_a}{v_m}\right)^{-\frac{p-1}{2}} \left(\frac{v}{v_a}\right)^{\frac{5}{2}} \propto t^{\frac{11}{2(5-k)}} v^{\frac{5}{2}}, & v_m < v < v_a \\ \left(\frac{v}{v_m}\right)^{-\frac{p-1}{2}} \propto t^{\frac{21-8k+4kp-15p}{2(5-k)}} v^{-\frac{p-1}{2}}, & v_a < v < v_c \\ \left(\frac{v_c}{v_m}\right)^{-\frac{p-1}{2}} \left(\frac{v}{v_c}\right)^{-\frac{p}{2}} \propto t^{\frac{20-6k+4kp-15p}{2(5-k)}} v^{-\frac{p}{2}}, & v_c < v \end{cases} \quad (24)$$

Our results return to those given by Gao et al. (2013) for $k=0$ and 2. We summarize α , β and their CRs as a function of k in Table 1. Therefore, the measurements of α and β , can be used to estimate the CNM density profile (k).

We show the CRs for different k and at different spectra regimes in Figure 2. The solid lines, dotted lines and dashed lines represent the CRs for outflow in the coasting phase, relativistic jet in the deceleration phase and non-relativistic outflows in deceleration phase, respectively. At high frequency, the CRs for different electron spectral index p are represented

Table 1. Closure relations (CRs) for an arbitrary CNM profile k at different spectra regime.

Phase	Spectra regime	β	$k_{CR}(\beta)$
Coasting	$v < v_a$	-2	$\frac{2\alpha_{CR}-\beta}{\beta}$
	$v_a < v < v_c$	$-\frac{1}{3}$	$\frac{11\beta-\alpha_{CR}}{6\beta}$
	$v_c < v < v_m$	$\frac{1}{2}$	$\frac{2\alpha_{CR}+8\beta}{3\beta}$
	$v_m < v$	$\frac{p}{2}$	$\frac{2\alpha_{CR}+4}{\beta+1}$
	$v < v_a$	-2	-
	$v_a < v < v_m$	$-\frac{1}{3}$	$\frac{9\beta-\alpha_{CR}}{4\beta}$
	$v_m < v < v_c$	$\frac{p-1}{2}$	$\frac{2\alpha_{CR}+6}{3+\beta}$
	$v_c < v$	$\frac{p}{2}$	$\frac{2\alpha_{CR}+4}{1+\beta}$
	$v < v_m$	-2	-
	$v_m < v < v_a$	$-\frac{5}{2}$	$\frac{10\alpha_{CR}-8\beta}{\beta}$
$v_a < v < v_c$	$\frac{p-1}{2}$	$\frac{2\alpha_{CR}+6}{3+\beta}$	
$v_c < v$	$\frac{p}{2}$	$\frac{2\alpha_{CR}+4}{1+\beta}$	
BM deceleration	$v < v_a$	-2	$\frac{4\alpha_{CR}-2\beta}{\alpha_{CR}}$
	$v_a < v < v_c$	$-\frac{1}{3}$	$\frac{4\alpha_{CR}-2\beta}{\alpha_{CR}-3\beta}$
	$v_c < v < v_m$	$\frac{1}{2}$	-
	$v_m < v$	$\frac{p}{2}$	-
	$v < v_a$	-2	$\frac{4\alpha_{CR}-\beta}{\alpha_{CR}}$
	$v_a < v < v_m$	$-\frac{1}{3}$	$\frac{4\alpha_{CR}-6\beta}{\alpha_{CR}-3\beta}$
	$v_m < v < v_c$	$\frac{p-1}{2}$	$\frac{8\alpha_{CR}-12\beta}{2\alpha_{CR}-3\beta+1}$
	$v_c < v$	$\frac{p}{2}$	-
	$v < v_m$	-2	$\frac{4\alpha_{CR}-\beta}{\alpha_{CR}}$
	$v_m < v < v_a$	$-\frac{5}{2}$	$\frac{40\alpha_{CR}-20\beta}{10\alpha_{CR}-3\beta}$
$v_a < v < v_c$	$\frac{p-1}{2}$	$\frac{8\alpha_{CR}-12\beta}{2\alpha_{CR}-3\beta+1}$	
$v_c < v$	$\frac{p}{2}$	-	
ST deceleration	$v < v_a$	-2	$\frac{5\alpha_{CR}+\beta}{\alpha_{CR}+\beta}$
	$v_a < v < v_m$	$-\frac{1}{3}$	$\frac{5\alpha_{CR}-24\beta}{\alpha_{CR}-10\beta}$
	$v_m < v < v_c$	$\frac{p-1}{2}$	$\frac{5\alpha_{CR}-15\beta+3}{\alpha_{CR}-4\beta+2}$
	$v_c < v$	$\frac{p}{2}$	$\frac{5\alpha_{CR}-15\beta+10}{\alpha_{CR}-4\beta+3}$
	$v < v_m$	-2	$\frac{5\alpha_{CR}+\beta}{\alpha_{CR}+\beta}$
	$v_m < v < v_a$	$-\frac{5}{2}$	$\frac{25\alpha_{CR}-11\beta}{5\alpha_{CR}}$
	$v_a < v < v_c$	$\frac{p-1}{2}$	$\frac{5\alpha_{CR}-15\beta+3}{\alpha_{CR}-4\beta+2}$
	$v_c < v$	$\frac{p}{2}$	$\frac{5\alpha_{CR}-15\beta+10}{\alpha_{CR}-4\beta+3}$

by different colors, where red, green, blue, and magenta represent $p = 2.01, 2.5, 3$ and 3.5 , respectively. From Figure 2, we find that CRs at $v < v_a < v_m < v_c$ and $v < v_m < v_a < v_c$ for the coasting phase and $v_a < v_c < v < v_m$, $v_a < v_c < v_m < v$, $v_a < v_m < v_c < v$ and $v_m < v_a < v_c < v$ for the deceleration phase of a relativistic outflow are independent of the CNM density profile k , which means that we cannot infer the CNM density profile through these CRs. Fortu-

nately, most TDEs are during the coasting phase and have been well observed in high frequencies. Additionally, within the same dynamical phase, for the cases where $v_a < v_m < v_c$ and $v_m < v_a < v_c$, the CRs for each spectral segment (with the exception of the second spectral segment) are correspondingly identical. The three characteristic frequencies of radio emissions from all current TDEs fall within these two cases, thus greatly reducing the impact of the judgment of the case on our CRs results.

3.2. Method

In this section, we describe the specific methods used for the CR analysis, including the spectral and light curve fitting procedures.

3.2.1. Spectra fitting

We fit the radio spectra of each TDE with the models developed by [Granot et al. \(2002\)](#). For $v_a < v_m < v_c$, the spectrum can be described with

$$F_1 = F_V(v_a) \left[\left(\frac{\nu}{v_a} \right)^{s_1 \beta_1} + \left(\frac{\nu}{v_a} \right)^{s_1 \beta_2} \right]^{-1/s_1} \times \left[1 + \left(\frac{\nu}{v_m} \right)^{s_2(\beta_2 - \beta_3)} \right]^{-1/s_2}, \quad (25)$$

where $\beta_1 = -2$, $\beta_2 = -1/3$ and $\beta_3 = (p-1)/2$ are the spectra index, and s_1 and s_2 are smoothing parameters. For $v_m < v_a < v_c$, the spectrum can be given by

$$F_2 = F_V(v_m) \left[\left(\frac{\nu}{v_m} \right)^2 \exp \left(-s_3 \left(\frac{\nu}{v_m} \right)^{2/3} \right) + \left(\frac{\nu}{v_m} \right)^{5/2} \right] \times \left[1 + \left(\frac{\nu}{v_a} \right)^{s_4(\beta_3 - \beta_2)} \right]^{-1/s_4}, \quad (26)$$

where $\beta_2 = -5/2$ and $\beta_3 = (p-1)/2$, and s_3 and s_4 are smoothing parameters.

For some TDEs like AT2020vwl ([Goodwin et al. 2023b, 2025b](#)), ASASSN-14li ([Alexander et al. 2016](#)) and AT2020wjw ([Goodwin et al. 2024](#)), their radio emission also includes a host-galaxy component, we adopt it as

$$F_{V,\text{host}} = F_0 \left(\frac{\nu}{1.4 \text{ GHz}} \right)^{\alpha_0}, \quad (27)$$

where F_0 is the flux density of the host galaxy at 1.4 GHz, α_0 is the spectra index of the host galaxy. For these sources, the data are fitted with models of the form $F_1 + F_{V,\text{host}}$ (for $v_a < v_m$) or $F_2 + F_{V,\text{host}}$ (for $v_m < v_a$).

We derived the best fit by using a Python implementation of Markov Chain Monte Carlo (MCMC), `emcee` ([Foreman-Mackey et al. 2013](#)). The parameter ranges are constrained as follows: F_V is limited to $10^{-4} - 100$ mJy, F_0 are limited

to $10^{-4} - 2$ mJy, α_0 is limited to $-2 - 0$, p is limited to $2.0 - 4.0$, and the ranges of v_a and v_m are set according to the spectral properties of each individual source. For each MCMC calculation, we employed $\max(2n_{dim}, 50)$ walkers (n_{dim} denotes the number of free parameters), 20000 steps, and discarding the first 10000 steps. In our fitting procedure, the values of F_0 , α_0 and p are determined from a joint fit to all available spectra of the source. The resulting values for p and the spectra index relevant to our CR analysis are listed in Table 2, including the median value from the posterior distribution and the 16th and 84th percentiles, correspond to approximately 1σ errors.

3.2.2. Light curve fitting

Based on the spectral-fitting results, we logarithmically sampled 500 frequencies across the observational band for each SED and computed the corresponding model fluxes. Subsequently, we performed a power-law fit on the light curves at 500 sampled frequencies to obtain the frequency-dependent distribution of the temporal index.

We prefer to obtain α_{CR} by fitting the light curves of the lower ($< \min(v_a, v_m)$) or higher ($> \max(v_a, v_m)$) frequencies, since these frequencies are usually located at the same spectral regime (we don't need to consider the transition of α due to crossing of the peak frequency, i.e., v_a or v_m). For each frequency, we obtain a temporal index α from its light curve. The resulting α_{CR} of a TDE is the average of all these temporal indices. Substituting α_{CR} and β_{CR} into the analytical expression of CR allows us to infer the density profile of the CNM.

4. RESULTS AND DISCUSSIONS

For the 53 radio TDEs collected, we selected those suitable for CR analysis based on the following criteria: (1) at least two SEDs are available; and (2) at least two SEDs containing more than three data points.

Applying these criteria, we yield a sample of 26 TDEs to constrain the CNM density profile index with the CR analysis. There are three typical cases: (1) AT2022cmc is the only TDE in our sample for which the CR analysis requires a relativistic deceleration phase. (2) CNSS J0019+00 represents the typical behavior of most radio TDEs, with a non-relativistic outflow in the coasting phase. (3) ASASSN-14li exhibits radio emission that includes not only the synchrotron component but also a contribution from its host galaxy. The spectra fitting of these three TDEs are presented in Figure 3.

For AT2022cmc, most of its SEDs are in the low-frequency regime (corresponding to a spectral index of $\beta_{\text{CR}} = -2$), we obtain the mean temporal index $\alpha_{\text{CR}} = -0.75 \pm 0.02$ from the light curves of this low-frequency range ($\nu < v_a < v_m < v_c$). Assuming the outflow is in the BM deceleration phase, the CR analysis yields a CNM density profile of $k_{\text{CR}} = 1.35 \pm$

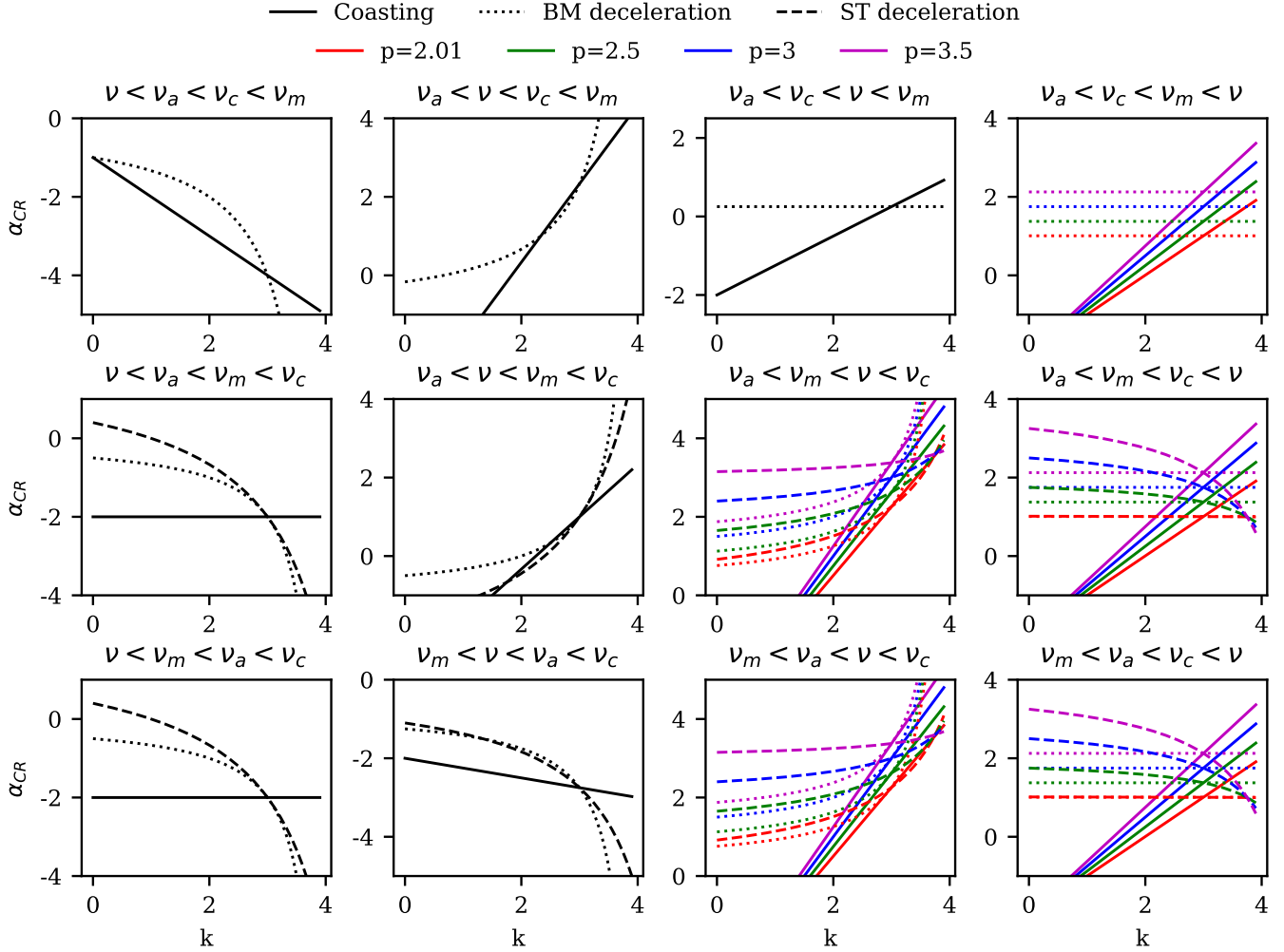


Figure 2. The relation between temporal index α_{CR} and the CNM density profile k for $\nu_a < \nu_c < \nu_m$ (top), $\nu_a < \nu_m < \nu_c$ (middle), and $\nu_m < \nu_a < \nu_c$ (bottom). The solid lines and dotted lines represent the coasting phase and the deceleration phase of relativistic outflow. Different colored lines represent different electron spectral index p , where red, green, blue, magenta and gray represent $p = 2.01, 2.5, 3.0$ and 3.5 , respectively. When the relativistic outflow is in the deceleration phase, the CNM density profile cannot be derived from the CRs at high frequencies ($\nu_a < \nu_c < \nu < \nu_m$, $\nu_a < \nu_c < \nu_m < \nu$, $\nu_a < \nu_m < \nu_c < \nu$, and $\nu_m < \nu_a < \nu_c < \nu$). When the outflow is in the coasting phase, the CNM density profile cannot be derived from the CRs at low frequencies ($\nu < \nu_a < \nu_m < \nu_c$ and $\nu < \nu_m < \nu_a < \nu_c$).

0.06, which is consistent with our previous work (Zhou et al. 2024). For other TDEs, we use the light curve in the high-frequency regime.

The results of the CNM density profile of these 26 TDEs are presented in Table 2. The distribution of k_{CR} is shown in Figure 4.

4.1. Negative profile index

Three TDEs in our sample, i.e., ASASSN-14ae, AT2018hyz, and eRASSt J011431-593654 exhibit negative CNM density slopes ($k < 0$), indicating an unreasonable inverted density profile.

ASASSN-14ae has two SEDs at 2696 and 3243 day, suggesting an electron spectral index of $p = 2.01 \pm 0.01$. The average temporal index is $\alpha_{CR} = -4.96 \pm 0.05$, and the cor-

responding spectral index is $\beta_{CR} = 0.50 \pm 0.01$. We obtain a CNM density profile of $k_{CR} = -1.12 \pm 0.03$ during the coasting phase by CR analysis. AT2018hyz was modeled using 16 SEDs spanning 1125–2160 days, and the spectral fitting yields $p = 2.01 \pm 0.01$. The average temporal index is $\alpha_{CR} = -3.97 \pm 0.04$, and the corresponding spectral index is $\beta_{CR} = (p - 1)/2 = 0.50 \pm 0.00$. We obtain a CNM density profile of $k_{CR} = -0.55 \pm 0.02$ during the coasting phase by CR analysis. eRASSt J011431-593654 was modeled by fitting two SEDs at 1224 and 1415 days, yielding $p = 3.42 \pm 0.60$. The light curves at high-frequencies show an average temporal index of $\alpha_{CR} = -3.77 \pm 0.29$, with a corresponding spectral index of $\beta_{CR} = (p - 1)/2 = 1.21 \pm 0.30$. By substituting these two parameters into the CR expression,

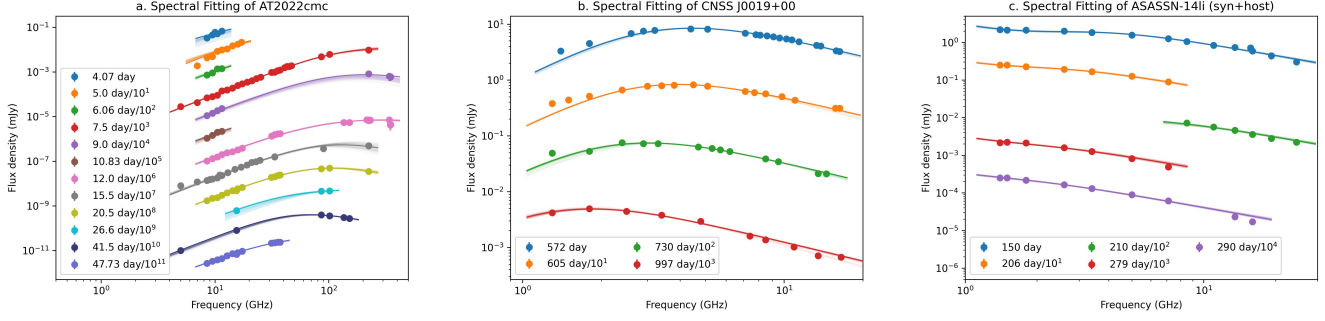


Figure 3. Radio SEDs for AT2022cmc, CNSS J0019+00, and ASASSN-14li. These lines represent the best-fit model from the MCMC fitting and some randomly sampled MCMC lines.

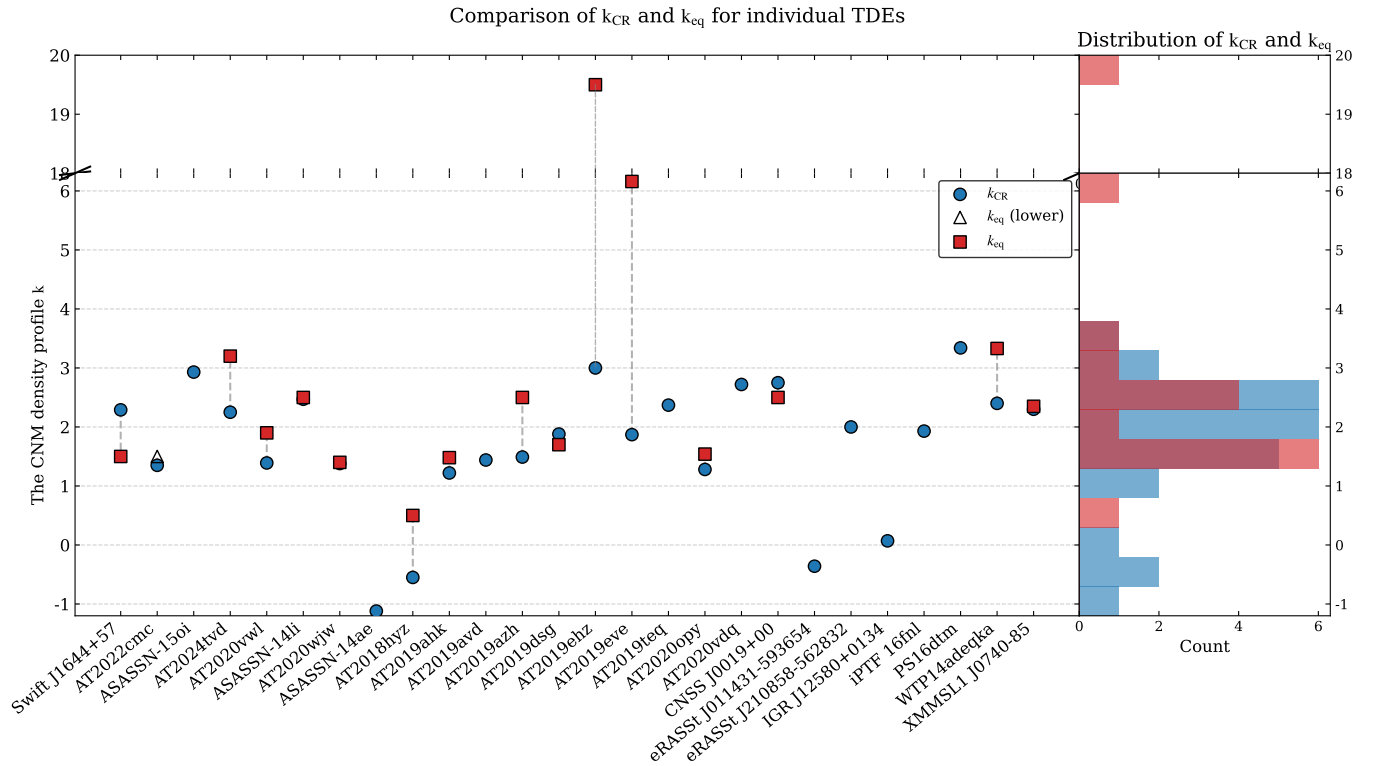


Figure 4. Left panel: The CNM density profile for our TDE sample, as inferred from equipartition and CRs. Right panel: The distributions of the CNM density profile k_{CR} and k_{eq} , along with the Gaussian curves fitted to their distributions.

we obtain a CNM density profile of $k_{CR} = -0.36 \pm 0.14$ during the coasting phase.

Matsumoto & Piran (2024) explored a model of a changed CNM density profile that initially decreases as a power-law with radius but tends to a constant value beyond the Bondi radius, which can explain the delayed radio emission. In this model, after entering a constant-density medium, the growth of radio emission over time with $L_v \propto t^3$, which is determined by the cubic relation between the number of swept-up electrons and the radius ($N_e \propto R^3$) and the fact that the outflow propagates at a constant velocity before deceleration

($R \propto t$). Therefore, this model struggles to explain the steep rise ($\alpha_{CR} < -3$) light curve as in AT2018hyz.

Recently, several works suggested that the late-time fast rising can be produced when the outflow encounters surrounding gaseous clouds or a torus (Mou & Wang 2021; Mou et al. 2022; Bu et al. 2023; Lei et al. 2024; Zhuang et al. 2025). Lei et al. (2024) proposed a model investigating the interaction between the unbound debris and the external dusty torus commonly found in galactic nuclear regions, particularly in active galactic nuclei. Using three-dimensional hydrodynamic simulations with the Athena++ code, their results show that the debris-torus collision generates strongly

Table 2. Parameters of the CR analysis.

TDE	β_{CR}	p	α_{CR}	k_{CR}	k_{eq}
Swift J1644+57	1.47 ± 0.01	3.94 ± 0.03	2.11 ± 0.02	2.29 ± 0.01^a	1.5 (Eftekhari et al. 2018)
AT2022cmc	−2	3.47 ± 0.26	-0.75 ± 0.02	1.35 ± 0.06^b	1.5 − 2 (Matsumoto & Metzger 2023)
ASASSN-15oi	0.79 ± 0.02	2.58 ± 0.03	2.55 ± 0.09	2.93 ± 0.05^a	− ^c (Hajela et al. 2025)
AT2024tvd	0.58 ± 0.05	2.16 ± 0.09	1.03 ± 0.26	2.25 ± 0.15^a	3.20 ^d (Sfaradi et al. 2025b)
AT2020vwl	1.43 ± 0.07	3.87 ± 0.14	0.09 ± 0.16	1.39 ± 0.07^a	1.90 ^d (Goodwin et al. 2025b)
ASASSN-14li	1.13 ± 0.07	3.25 ± 0.14	2.10 ± 0.20	2.47 ± 0.11^a	2.5 (Alexander et al. 2016)
AT2020wjw	1.46 ± 0.04	3.93 ± 0.08	0.07 ± 0.03	1.38 ± 0.02^a	1.4 (Goodwin et al. 2024)
ASASSN-14ae	0.50 ± 0.01	2.01 ± 0.01	-4.96 ± 0.05	-1.12 ± 0.03^a	− ^c (Cendes et al. 2024c)
AT2018hyz	0.50 ± 0.00	2.01 ± 0.01	-3.97 ± 0.04	-0.55 ± 0.02^a	0.5 (Cendes et al. 2025)
AT2019ahk	1.16 ± 0.09	3.31 ± 0.17	-0.47 ± 0.03	1.22 ± 0.03^a	1.48 ^d (Christy et al. 2024a)
AT2019avd	1.16 ± 0.22	3.33 ± 0.44	0.00 ± 0.01	1.44 ± 0.08^a	− ^c
AT2019azh	1.03 ± 0.01	3.07 ± 0.02	0.00 ± 0.00	1.49 ± 0.00^a	2.5 (Goodwin et al. 2022)
AT2019dsg	1.48 ± 0.02	3.96 ± 0.04	1.21 ± 0.03	1.88 ± 0.01^a	1.7 (Cendes et al. 2021a)
AT2019ehz	1.47 ± 0.03	3.94 ± 0.06	3.72 ± 0.09	3.00 ± 0.05^a	19.50 ^d (Cendes et al. 2024c)
AT2019eve	1.02 ± 0.03	3.04 ± 0.06	0.75 ± 0.09	1.87 ± 0.04^a	6.16 ^d (Cendes et al. 2024c)
AT2019teq	1.39 ± 0.11	3.77 ± 0.23	2.19 ± 0.08	2.37 ± 0.07^a	− ^c (Cendes et al. 2024c)
AT2020opy	1.10 ± 0.14	3.20 ± 0.28	-0.38 ± 0.07	1.28 ± 0.06^a	1.54 ^d (Goodwin et al. 2023a)
AT2020vdq	1.17 ± 0.09	3.35 ± 0.19	2.67 ± 0.10	2.72 ± 0.08^a	−
CNSS J0019+00	1.14 ± 0.04	3.29 ± 0.08	2.69 ± 0.10	2.75 ± 0.05^a	2.5 (Anderson et al. 2020)
eRASSt J011431-593654	1.21 ± 0.30	3.42 ± 0.60	-3.77 ± 0.29	-0.36 ± 0.14^a	− ^c (Goodwin et al. 2025a)
eRASSt J210858-562832	1.43 ± 0.07	3.85 ± 0.13	1.42 ± 0.13	2.00 ± 0.07^a	− ^c (Goodwin et al. 2025a)
IGR J12580+0134	1.48 ± 0.03	3.96 ± 0.06	-2.85 ± 0.17	0.07 ± 0.08^a	− ^c
iPTF 16fnl	1.30 ± 0.18	3.60 ± 0.35	1.14 ± 0.45	1.93 ± 0.22^a	− ^c (Cendes et al. 2024c)
PS16dtm	0.65 ± 0.07	2.31 ± 0.14	3.10 ± 0.09	3.34 ± 0.08^a	− ^c (Cendes et al. 2024c)
WTP14adeqka	0.76 ± 0.00	2.53 ± 0.00	1.52 ± 0.09	2.40 ± 0.05^a	3.33 ^d (Golay et al. 2025)
XMMSL1 J0740-85	1.10 ± 0.20	3.19 ± 0.40	1.71 ± 0.28	2.30 ± 0.18^a	2.35 (Alexander et al. 2017)

^a The CNM density profile at Coasting phase.

^b The CNM density profile at BM deceleration phase.

^c Due to the lack of peak SED observations, it is difficult to constrain k_{eq} .

^d k_{eq} is obtained by performing linear fitting on the equipartition results from other work.

shocked material, and the resulting radio emission exhibits a characteristic light curve with a sharp rise and slow decay. Zhuang et al. (2025) proposed an outflow-cloud interaction model to explain the late-time radio flare in AT2018hyz. In his model, a sub-relativistic outflow generated at early stages collides with discrete, dense clouds located on scales of 0.1–1 pc during its propagation, forming bow shocks that produce radio flares through synchrotron radiation. This naturally ex-

plains both the time delay (several years) of the late flare in AT2018hyz and the steep rise of its light curve. Therefore, the negative density profile indices might be the encounter of dense medium such as a cloud or torus.

4.2. Compared with equipartition method

In table 2, we also present the equipartition values k_{eq} obtained from the literature. The comparison of these two val-

ues, i.e., k_{CR} and k_{eq} , and the distributions are shown in Figure 4.

As we can see, the results of the two methods are generally consistent, with the CNM density profiles predominantly concentrated around $k = 2$. However, two TDEs, namely AT2019ehz and AT2019eve, exhibit significant discrepancies between the two methods.

For CR analysis, AT2019ehz uses 2 SEDs on 970 and 1262 days. We obtain $p = 3.94 \pm 0.06$ by the spectral fitting. The average temporal index is $\alpha_{\text{CR}} = 3.72 \pm 0.09$, with a corresponding spectral index of $\beta_{\text{CR}} = (p - 1)/2 = 1.47 \pm 0.03$. By substituting these two parameters into the CR expression, we obtain a CNM density profile of $k_{\text{CR}} = 3.00 \pm 0.05$ during the coasting phase. For AT2019eve, we use 3 SEDs that include 945, 1092 and 1325 days. We then get $p = 3.04 \pm 0.06$, an average temporal index of $\alpha_{\text{CR}} = 0.75 \pm 0.09$, and the corresponding spectral index of $\beta_{\text{CR}} = (p - 1)/2 = 1.02 \pm 0.03$. With CR expression, we obtain a CNM density profile of $k_{\text{CR}} = 1.87 \pm 0.04$ during the coasting phase.

The CNM density slopes derived from the equipartition method are $k_{\text{eq}} = 19.50$ and $k_{\text{eq}} = 6.16$ for AT2019ehz and AT2019eve, respectively (Cendes et al. 2024c). The large discrepancies with the results of CR analysis lie in the fact that poor data are used. For both cases, the values of k_{eq} are obtained from only two or three time epochs. There are large uncertainties induced, since k_{eq} is usually variable with radius (and time). The equipartition method highly relies on the measurements of the peak frequency (ν_a or ν_m), which introduce additional error with the poor SEDs in AT2019ehz and AT2019eve.

5. SUMMARY

With the rapid increase in radio observations of TDEs, and given that their radio emission is generally produced by the interaction between an outflow and the surrounding circumnuclear medium (CNM), radio-detected TDEs have become a powerful probe of the CNM density profile. In this work, we collect the TDEs with radio observations and constrain the CNM density profile with CR analysis. The main results of this work are summarized as follows:

1. We obtain a sample of 53 TDEs with long-term radio observations, including 14 X-ray (or gamma-ray) se-

lected TDEs, 34 optical selected TDEs, 3 infrared selected TDEs and 2 radio selected TDEs. There are only five TDEs with a relativistic jet. For AT2019teq and AT2020vdq, we reduce the VLA data following standard procedures using the CASA package. This TDE sample enables us to carry out a comprehensive study of the CNM of dormant SMBHs.

2. We present the CR expressions for the synchrotron emission from the interaction of outflow with an arbitrary CNM, establishing the relationship between the CNM density profile index k and the temporal index α (given the spectral index β). This provides a theoretical framework for constraining CNM properties using radio data.
3. We select 26 TDEs from the sample that suitable for CR analysis, and obtain CNM profile with the CR method. We find that our results are generally consistent with that from equipartition method, indicating that CR analysis remains a powerful diagnostic of the CNM profile.

This study presents an efficient method for estimating the CNM density profile.

Future facilities, like FAST Core Array (Jiang et al. 2024), with higher sensitivity and resolution are expected to collect rich radio data for TDEs, which will advance our understanding of the CNM environments of quiescent SMBHs.

ACKNOWLEDGMENTS

We thank the participants of the TDE FORUM (Full-process Orbital to Radiative Unified Modeling) online seminar series for their inspiring discussions. We are very grateful to Yanan Wang, Rongfeng Shen, Xinwen Shu, Bing Zhang, Erlin Qiao, Tao An, Agnieszka Janiuk, and Chichuan Jin for their helpful discussions. This work is supported by the National Natural Science Foundation of China under grants 12473012 and 12533005, the National Key R&D Program of China (Nos. 2023YFC2205901), and the Fundamental Research Funds for the Central Universities, HUST (No. YCJJ20252115). The authors acknowledge Beijing PARATERA Tech CO., Ltd. for providing HPC resources that have contributed to the research results reported within this paper.

REFERENCES

- Alexander, K. D., Berger, E., Guillochon, J., Zauderer, B. A., & Williams, P. K. G. 2016, *ApJL*, 819, L25, doi: [10.3847/2041-8205/819/2/L25](https://doi.org/10.3847/2041-8205/819/2/L25)
- Alexander, K. D., van Velzen, S., Horesh, A., & Zauderer, B. A. 2020, *SSRv*, 216, 81, doi: [10.1007/s11214-020-00702-w](https://doi.org/10.1007/s11214-020-00702-w)
- Alexander, K. D., Wieringa, M. H., Berger, E., Saxton, R. D., & Komossa, S. 2017, *ApJ*, 837, 153, doi: [10.3847/1538-4357/aa6192](https://doi.org/10.3847/1538-4357/aa6192)
- Alexander, K. D., Margutti, R., Gomez, S., et al. 2025, arXiv e-prints, arXiv:2506.12729, doi: [10.48550/arXiv.2506.12729](https://doi.org/10.48550/arXiv.2506.12729)

- Anderson, M. M., Mooley, K. P., Hallinan, G., et al. 2020, *ApJ*, 903, 116, doi: [10.3847/1538-4357/abb94b](https://doi.org/10.3847/1538-4357/abb94b)
- Andreoni, I., Coughlin, M. W., Perley, D. A., et al. 2022, *Nature*, 612, 430, doi: [10.1038/s41586-022-05465-8](https://doi.org/10.1038/s41586-022-05465-8)
- Angus, C. R., Baldassare, V. F., Mockler, B., et al. 2022, *Nature Astronomy*, 6, 1452, doi: [10.1038/s41550-022-01811-y](https://doi.org/10.1038/s41550-022-01811-y)
- Anumarlapudi, A., Dobie, D., Kaplan, D. L., et al. 2024, *ApJ*, 974, 241, doi: [10.3847/1538-4357/ad64d3](https://doi.org/10.3847/1538-4357/ad64d3)
- Arcavi, I., Burke, J., Nyiha, I., & Nicholl, M. 2020, *Transient Name Server AstroNote*, 202, 1
- Arcavi, I., Faris, S., Newsome, M., Sniegowska, M., & Trakhtenbrot, B. 2024, *Transient Name Server AstroNote*, 53, 1
- Arcavi, I., Dgany, Y., Pellegrino, C., et al. 2022, *Transient Name Server Classification Report*, 2022-504, 1
- Baganoff, F. K., Maeda, Y., Morris, M., et al. 2003, *ApJ*, 591, 891, doi: [10.1086/375145](https://doi.org/10.1086/375145)
- Barniol Duran, R., Nakar, E., & Piran, T. 2013, *ApJ*, 772, 78, doi: [10.1088/0004-637X/772/1/78](https://doi.org/10.1088/0004-637X/772/1/78)
- Berger, E., Zauderer, A., Pooley, G. G., et al. 2012, *ApJ*, 748, 36, doi: [10.1088/0004-637X/748/1/36](https://doi.org/10.1088/0004-637X/748/1/36)
- Blanchard, P. K., Nicholl, M., Berger, E., et al. 2017, *ApJ*, 843, 106, doi: [10.3847/1538-4357/aa77f7](https://doi.org/10.3847/1538-4357/aa77f7)
- Blandford, R. D., & McKee, C. F. 1976, *Physics of Fluids*, 19, 1130, doi: [10.1063/1.861619](https://doi.org/10.1063/1.861619)
- Bloom, J. S., Giannios, D., Metzger, B. D., et al. 2011, *Science*, 333, 203, doi: [10.1126/science.1207150](https://doi.org/10.1126/science.1207150)
- Bondi, H. 1952, *MNRAS*, 112, 195, doi: [10.1093/mnras/112.2.195](https://doi.org/10.1093/mnras/112.2.195)
- Bright, A. J., Carotenuto, F., & Jonker, P. G. 2025, *GRB Coordinates Network*, 40985, 1
- Bright, J. S., Fender, R. P., Motta, S. E., et al. 2018, *MNRAS*, 475, 4011, doi: [10.1093/mnras/sty077](https://doi.org/10.1093/mnras/sty077)
- Brimacombe, J., Kendurkar, M. R., Masi, G., et al. 2019, *The Astronomer's Telegram*, 12526, 1
- Brown, G. C., Levan, A. J., Stanway, E. R., et al. 2015, *MNRAS*, 452, 4297, doi: [10.1093/mnras/stv1520](https://doi.org/10.1093/mnras/stv1520)
- . 2017, *MNRAS*, 472, 4469, doi: [10.1093/mnras/stx2193](https://doi.org/10.1093/mnras/stx2193)
- Bu, D.-F., Chen, L., Mou, G., Qiao, E., & Yang, X.-H. 2023, *MNRAS*, 521, 4180, doi: [10.1093/mnras/stad804](https://doi.org/10.1093/mnras/stad804)
- Burn, M., Goodwin, A. J., Anderson, G. E., et al. 2025, *ApJ*, 993, 207, doi: [10.3847/1538-4357/ae0a16](https://doi.org/10.3847/1538-4357/ae0a16)
- Bykov, S. D., Gilfanov, M. R., & Sunyaev, R. A. 2024, *MNRAS*, 527, 1962, doi: [10.1093/mnras/stad3355](https://doi.org/10.1093/mnras/stad3355)
- Cannizzaro, G., Wevers, T., Jonker, P. G., et al. 2021, *MNRAS*, 504, 792, doi: [10.1093/mnras/stab851](https://doi.org/10.1093/mnras/stab851)
- Cendes, Y., Alexander, K. D., Berger, E., et al. 2021a, *ApJ*, 919, 127, doi: [10.3847/1538-4357/ac110a](https://doi.org/10.3847/1538-4357/ac110a)
- Cendes, Y., Berger, E., Alexander, K., Laskar, T., & Goodwin, A. 2024a, *The Astronomer's Telegram*, 16650, 1
- . 2024b, *The Astronomer's Telegram*, 16650, 1
- Cendes, Y., Eftekhari, T., Berger, E., & Polisensky, E. 2021b, *ApJ*, 908, 125, doi: [10.3847/1538-4357/abd323](https://doi.org/10.3847/1538-4357/abd323)
- Cendes, Y., Berger, E., Alexander, K. D., et al. 2022, *ApJ*, 938, 28, doi: [10.3847/1538-4357/ac88d0](https://doi.org/10.3847/1538-4357/ac88d0)
- . 2024c, *ApJ*, 971, 185, doi: [10.3847/1538-4357/ad5541](https://doi.org/10.3847/1538-4357/ad5541)
- Cendes, Y., Berger, E., Beniamini, P., et al. 2025, *arXiv e-prints*, arXiv:2507.08998, doi: [10.48550/arXiv.2507.08998](https://doi.org/10.48550/arXiv.2507.08998)
- Cenko, S. B., Krimm, H. A., Horesh, A., et al. 2012, *ApJ*, 753, 77, doi: [10.1088/0004-637X/753/1/77](https://doi.org/10.1088/0004-637X/753/1/77)
- Charalampopoulos, P., Leloudas, G., Pursiainen, M., & Kotak, R. 2023, *Transient Name Server AstroNote*, 115, 1
- Chen, T. W., Smith, K. W., Srivastav, S., et al. 2021, *Transient Name Server AstroNote*, 300, 1
- Cheng, H. Q., Zhao, G. Y., Zhou, C., et al. 2025, *The Astronomer's Telegram*, 17261, 1
- Christy, C. T., Alexander, K. D., Margutti, R., et al. 2024a, *ApJ*, 974, 18, doi: [10.3847/1538-4357/ad675b](https://doi.org/10.3847/1538-4357/ad675b)
- Christy, C. T., Alexander, K. D., Franz, N., et al. 2024b, *Transient Name Server AstroNote*, 56, 1
- Coughlin, E. R., & Begelman, M. C. 2014, *ApJ*, 781, 82, doi: [10.1088/0004-637X/781/2/82](https://doi.org/10.1088/0004-637X/781/2/82)
- Dai, J. L., Lodato, G., & Cheng, R. 2021, *SSRv*, 217, 12, doi: [10.1007/s11214-020-00747-x](https://doi.org/10.1007/s11214-020-00747-x)
- Dai, L., McKinney, J. C., Roth, N., Ramirez-Ruiz, E., & Miller, M. C. 2018, *ApJL*, 859, L20, doi: [10.3847/2041-8213/aab429](https://doi.org/10.3847/2041-8213/aab429)
- Eftekhari, T., Berger, E., Zauderer, B. A., Margutti, R., & Alexander, K. D. 2018, *ApJ*, 854, 86, doi: [10.3847/1538-4357/aaa8e0](https://doi.org/10.3847/1538-4357/aaa8e0)
- Evans, P. A., Campana, S., & Page, K. L. 2022, *The Astronomer's Telegram*, 15454, 1
- Faris, S., Arcavi, I., Newsome, M., et al. 2024, *Transient Name Server Classification Report*, 2024-4005, 1
- Foreman-Mackey, D., Hogg, D. W., Lang, D., & Goodman, J. 2013, *PASP*, 125, 306, doi: [10.1086/670067](https://doi.org/10.1086/670067)
- Forster, F. 2019, *Transient Name Server Discovery Report*, 2019-1857, 1
- Frajia, N., Kamenetskaia, B. B., Dainotti, M. G., et al. 2021, *ApJ*, 907, 78, doi: [10.3847/1538-4357/abcaf6](https://doi.org/10.3847/1538-4357/abcaf6)
- Frederick, S., Gezari, S., Velzen, S. V., et al. 2020, *Transient Name Server AstroNote*, 143, 1
- Fremling, C. 2024, *Transient Name Server Discovery Report*, 2024-135, 1
- Gao, H., Lei, W.-H., Zou, Y.-C., Wu, X.-F., & Zhang, B. 2013, *NewAR*, 57, 141, doi: [10.1016/j.newar.2013.10.001](https://doi.org/10.1016/j.newar.2013.10.001)
- Gezari, S., Perley, D., & Sollerman, J. 2020, *The Astronomer's Telegram*, 13944, 1
- Gezari, S., Hung, T., Blagorodnova, N., et al. 2016, *The Astronomer's Telegram*, 9433, 1
- Golay, W. W., Berger, E., Cendes, Y., et al. 2025, *arXiv e-prints*, arXiv:2508.16756, doi: [10.48550/arXiv.2508.16756](https://doi.org/10.48550/arXiv.2508.16756)

- Gomez, S., Nicholl, M., Short, P., et al. 2020, *MNRAS*, 497, 1925, doi: [10.1093/mnras/staa2099](https://doi.org/10.1093/mnras/staa2099)
- Gompertz, B. P., Levan, A. J., Laskar, T., et al. 2026, *ApJL*, 997, L4, doi: [10.3847/2041-8213/ae2ed9](https://doi.org/10.3847/2041-8213/ae2ed9)
- Goodwin, A. J., van Velzen, S., Miller-Jones, J. C. A., et al. 2022, *MNRAS*, 511, 5328, doi: [10.1093/mnras/stac333](https://doi.org/10.1093/mnras/stac333)
- Goodwin, A. J., Miller-Jones, J. C. A., van Velzen, S., et al. 2023a, *MNRAS*, 518, 847, doi: [10.1093/mnras/stac3127](https://doi.org/10.1093/mnras/stac3127)
- Goodwin, A. J., Alexander, K. D., Miller-Jones, J. C. A., et al. 2023b, *MNRAS*, 522, 5084, doi: [10.1093/mnras/stad1258](https://doi.org/10.1093/mnras/stad1258)
- Goodwin, A. J., Anderson, G. E., Miller-Jones, J. C. A., et al. 2024, *MNRAS*, 528, 7123, doi: [10.1093/mnras/stae362](https://doi.org/10.1093/mnras/stae362)
- Goodwin, A. J., Burn, M., Anderson, G. E., et al. 2025a, *ApJS*, 278, 36, doi: [10.3847/1538-4365/adbe80](https://doi.org/10.3847/1538-4365/adbe80)
- Goodwin, A. J., Mummery, A., Laskar, T., et al. 2025b, *ApJ*, 981, 122, doi: [10.3847/1538-4357/adb0b1](https://doi.org/10.3847/1538-4357/adb0b1)
- Granot, J., Panaitescu, A., Kumar, P., & Woosley, S. E. 2002, *ApJL*, 570, L61, doi: [10.1086/340991](https://doi.org/10.1086/340991)
- Gromadzki, M., Hamanowicz, A., Wyrzykowski, L., et al. 2019, *A&A*, 622, L2, doi: [10.1051/0004-6361/201833682](https://doi.org/10.1051/0004-6361/201833682)
- Guolo, M., Pasham, D. R., Zajaček, M., et al. 2024, *Nature Astronomy*, 8, 347, doi: [10.1038/s41550-023-02178-4](https://doi.org/10.1038/s41550-023-02178-4)
- Hajela, A., Alexander, K. D., Margutti, R., et al. 2025, *ApJ*, 983, 29, doi: [10.3847/1538-4357/adb620](https://doi.org/10.3847/1538-4357/adb620)
- Hammerstein, E., Chornock, R., Gezari, S., & Yao, Y. 2024, *Transient Name Server AstroNote*, 37, 1
- Hammerstein, E., van Velzen, S., Gezari, S., et al. 2023, *ApJ*, 942, 9, doi: [10.3847/1538-4357/aca283](https://doi.org/10.3847/1538-4357/aca283)
- Hinkle, J. T., Auchettl, K., Hoogendam, W. B., et al. 2024, arXiv e-prints, arXiv:2412.15326, doi: [10.48550/arXiv.2412.15326](https://doi.org/10.48550/arXiv.2412.15326)
- Holoien, T. W. S., Prieto, J. L., Bersier, D., et al. 2014, *MNRAS*, 445, 3263, doi: [10.1093/mnras/stu1922](https://doi.org/10.1093/mnras/stu1922)
- Holoien, T. W. S., Kochanek, C. S., Prieto, J. L., et al. 2016, *MNRAS*, 463, 3813, doi: [10.1093/mnras/stw2272](https://doi.org/10.1093/mnras/stw2272)
- Holoien, T. W. S., Huber, M. E., Shappee, B. J., et al. 2019a, *ApJ*, 880, 120, doi: [10.3847/1538-4357/ab2ae1](https://doi.org/10.3847/1538-4357/ab2ae1)
- Holoien, T. W. S., Vally, P. J., Auchettl, K., et al. 2019b, *ApJ*, 883, 111, doi: [10.3847/1538-4357/ab3c66](https://doi.org/10.3847/1538-4357/ab3c66)
- Holoien, T. W. S., Auchettl, K., Tucker, M. A., et al. 2020, *ApJ*, 898, 161, doi: [10.3847/1538-4357/ab9f3d](https://doi.org/10.3847/1538-4357/ab9f3d)
- Homan, D., Krumpke, M., Markowitz, A., et al. 2023, *A&A*, 672, A167, doi: [10.1051/0004-6361/202245078](https://doi.org/10.1051/0004-6361/202245078)
- Horesh, A., Bernstein, Y., Bright, J., et al. 2025, *Transient Name Server AstroNote*, 20, 1
- Horesh, A., Cenko, S. B., & Arcavi, I. 2021a, *Nature Astronomy*, 5, 491, doi: [10.1038/s41550-021-01300-8](https://doi.org/10.1038/s41550-021-01300-8)
- Horesh, A., Sfaradi, I., Fender, R., et al. 2021b, *ApJL*, 920, L5, doi: [10.3847/2041-8213/ac25fe](https://doi.org/10.3847/2041-8213/ac25fe)
- Horesh, A., Sfaradi, I., Bright, J., et al. 2018, *The Astronomer's Telegram*, 12271, 1
- Huang, B.-Q., & Liu, T. 2021, *ApJ*, 916, 71, doi: [10.3847/1538-4357/ac07a0](https://doi.org/10.3847/1538-4357/ac07a0)
- Hung, T., Cenko, S. B., Roth, N., et al. 2019, *ApJ*, 879, 119, doi: [10.3847/1538-4357/ab24de](https://doi.org/10.3847/1538-4357/ab24de)
- Hung, T., Foley, R. J., Ramirez-Ruiz, E., et al. 2020, *ApJ*, 903, 31, doi: [10.3847/1538-4357/abb606](https://doi.org/10.3847/1538-4357/abb606)
- Irwin, J. A., Henriksen, R. N., Krause, M., et al. 2015, *ApJ*, 809, 172, doi: [10.1088/0004-637X/809/2/172](https://doi.org/10.1088/0004-637X/809/2/172)
- Jiang, N., Wang, T., Yan, L., et al. 2017, *ApJ*, 850, 63, doi: [10.3847/1538-4357/aa93f5](https://doi.org/10.3847/1538-4357/aa93f5)
- Jiang, N., Wang, T., Dou, L., et al. 2021, *ApJS*, 252, 32, doi: [10.3847/1538-4365/abd1dc](https://doi.org/10.3847/1538-4365/abd1dc)
- Jiang, P., Chen, R., Gan, H., et al. 2024, *Astronomical Techniques and Instruments*, 1, 84, doi: [10.61977/ati2024012](https://doi.org/10.61977/ati2024012)
- Jose, J., Guo, Z., Long, F., et al. 2014, *The Astronomer's Telegram*, 6777, 1
- Lei, W.-H., Yuan, Q., Zhang, B., & Wang, D. 2016, *ApJ*, 816, 20, doi: [10.3847/0004-637X/816/1/20](https://doi.org/10.3847/0004-637X/816/1/20)
- Lei, X., Wu, Q., Li, H., et al. 2024, *ApJ*, 977, 63, doi: [10.3847/1538-4357/ad8ba5](https://doi.org/10.3847/1538-4357/ad8ba5)
- Leloudas, G., Dai, L., Arcavi, I., et al. 2019, *ApJ*, 887, 218, doi: [10.3847/1538-4357/ab5792](https://doi.org/10.3847/1538-4357/ab5792)
- Levan, A. J., Tanvir, N. R., Cenko, S. B., et al. 2011, *Science*, 333, 199, doi: [10.1126/science.1207143](https://doi.org/10.1126/science.1207143)
- Levan, A. J., Martin-Carrillo, A., Laskar, T., et al. 2025, *ApJL*, 990, L28, doi: [10.3847/2041-8213/adf8e1](https://doi.org/10.3847/2041-8213/adf8e1)
- Li, D., Zhang, W., Yang, J., et al. 2025, arXiv e-prints, arXiv:2509.25877, doi: [10.48550/arXiv.2509.25877](https://doi.org/10.48550/arXiv.2509.25877)
- Liodakis, I., Koljonen, K. I. I., Blinov, D., et al. 2023, *Science*, 380, 656, doi: [10.1126/science.abj9570](https://doi.org/10.1126/science.abj9570)
- Liu, T., Hou, S.-J., Xue, L., & Gu, W.-M. 2015, *ApJS*, 218, 12, doi: [10.1088/0067-0049/218/1/12](https://doi.org/10.1088/0067-0049/218/1/12)
- Liu, Z., Malyali, A., Krumpke, M., et al. 2023, *A&A*, 669, A75, doi: [10.1051/0004-6361/202244805](https://doi.org/10.1051/0004-6361/202244805)
- Liu, Z., Ryu, T., Goodwin, A. J., et al. 2024, *A&A*, 683, L13, doi: [10.1051/0004-6361/202348682](https://doi.org/10.1051/0004-6361/202348682)
- Malyali, A., Rau, A., Merloni, A., et al. 2021, *A&A*, 647, A9, doi: [10.1051/0004-6361/202039681](https://doi.org/10.1051/0004-6361/202039681)
- Malyali, A., Rau, A., Bonnerot, C., et al. 2024, *MNRAS*, 531, 1256, doi: [10.1093/mnras/stae927](https://doi.org/10.1093/mnras/stae927)
- Masterson, M., De, K., Panagiotou, C., et al. 2024, *ApJ*, 961, 211, doi: [10.3847/1538-4357/ad18bb](https://doi.org/10.3847/1538-4357/ad18bb)
- Matsumoto, T., & Metzger, B. D. 2023, arXiv e-prints, arXiv:2301.11939, doi: [10.48550/arXiv.2301.11939](https://doi.org/10.48550/arXiv.2301.11939)
- Matsumoto, T., & Piran, T. 2024, *ApJ*, 971, 49, doi: [10.3847/1538-4357/ad58ba](https://doi.org/10.3847/1538-4357/ad58ba)
- Mattila, S., Pérez-Torres, M., Efstathiou, A., et al. 2018, *Science*, 361, 482, doi: [10.1126/science.aao4669](https://doi.org/10.1126/science.aao4669)
- Mészáros, P., & Rees, M. J. 1997, *ApJ*, 476, 232, doi: [10.1086/303625](https://doi.org/10.1086/303625)

- Milán Veres, P., Franckowiak, A., van Velzen, S., et al. 2024, arXiv e-prints, arXiv:2408.17419, doi: [10.48550/arXiv.2408.17419](https://doi.org/10.48550/arXiv.2408.17419)
- Mohan, P., An, T., Zhang, Y., et al. 2022, *ApJ*, 927, 74, doi: [10.3847/1538-4357/ac4cb2](https://doi.org/10.3847/1538-4357/ac4cb2)
- Mou, G., Wang, T., Wang, W., & Yang, J. 2022, *MNRAS*, 510, 3650, doi: [10.1093/mnras/stab3742](https://doi.org/10.1093/mnras/stab3742)
- Mou, G., & Wang, W. 2021, *MNRAS*, 507, 1684, doi: [10.1093/mnras/stab2261](https://doi.org/10.1093/mnras/stab2261)
- Nicholl, M., Short, P., Angus, C., et al. 2019, *The Astronomer's Telegram*, 12752, 1
- Nicholl, M., Wevers, T., Oates, S. R., et al. 2020, *MNRAS*, 499, 482, doi: [10.1093/mnras/staa2824](https://doi.org/10.1093/mnras/staa2824)
- Nikołajuk, M., & Walter, R. 2013, *A&A*, 552, A75, doi: [10.1051/0004-6361/201220664](https://doi.org/10.1051/0004-6361/201220664)
- Nordin, J., Brinnet, V., Giomi, M., et al. 2020a, *Transient Name Server Discovery Report*, 2020-3103, 1
- . 2020b, *Transient Name Server Discovery Report*, 2020-3060, 1
- O'Brien, A., Kaplan, D., Murphy, T., Yu, W., & Zhang, W. 2019a, *The Astronomer's Telegram*, 13310, 1
- . 2019b, *The Astronomer's Telegram*, 13334, 1
- Pasham, D. R., Cenko, S. B., Levan, A. J., et al. 2015, *ApJ*, 805, 68, doi: [10.1088/0004-637X/805/1/68](https://doi.org/10.1088/0004-637X/805/1/68)
- Pasham, D. R., Lucchini, M., Laskar, T., et al. 2023, *Nature Astronomy*, 7, 88, doi: [10.1038/s41550-022-01820-x](https://doi.org/10.1038/s41550-022-01820-x)
- Perlman, E. S., Meyer, E. T., Wang, Q. D., et al. 2017, *ApJ*, 842, 126, doi: [10.3847/1538-4357/aa71b1](https://doi.org/10.3847/1538-4357/aa71b1)
- . 2022, *ApJ*, 925, 143, doi: [10.3847/1538-4357/ac3bba](https://doi.org/10.3847/1538-4357/ac3bba)
- Petrushevska, T., Leloudas, G., Ilić, D., et al. 2023, *A&A*, 669, A140, doi: [10.1051/0004-6361/202244623](https://doi.org/10.1051/0004-6361/202244623)
- Phinney, E. S. 1989, in *The Center of the Galaxy*, ed. M. Morris, Vol. 136, 543
- Planck Collaboration, Ade, P. A. R., Aghanim, N., et al. 2014, *A&A*, 571, A16, doi: [10.1051/0004-6361/201321591](https://doi.org/10.1051/0004-6361/201321591)
- Predehl, P., Andritschke, R., Arefiev, V., et al. 2021, *A&A*, 647, A1, doi: [10.1051/0004-6361/202039313](https://doi.org/10.1051/0004-6361/202039313)
- Qiao, E., Wu, Y., Lin, Y., et al. 2025, *MNRAS*, 539, 3473, doi: [10.1093/mnras/staf719](https://doi.org/10.1093/mnras/staf719)
- Ravi, V., Dykaar, H., Codd, J., et al. 2022, *ApJ*, 925, 220, doi: [10.3847/1538-4357/ac2b33](https://doi.org/10.3847/1538-4357/ac2b33)
- Rees, M. J. 1988, *Nature*, 333, 523, doi: [10.1038/333523a0](https://doi.org/10.1038/333523a0)
- Rees, M. J., & Meszaros, P. 1992, *MNRAS*, 258, 41, doi: [10.1093/mnras/258.1.41P](https://doi.org/10.1093/mnras/258.1.41P)
- Rhodes, L., Bright, J. S., Fender, R., et al. 2023, *MNRAS*, 521, 389, doi: [10.1093/mnras/stad344](https://doi.org/10.1093/mnras/stad344)
- Rybicki, G. B., & Lightman, A. P. 1979, *Radiative processes in astrophysics*
- Sari, R., Piran, T., & Narayan, R. 1998, *ApJL*, 497, L17, doi: [10.1086/311269](https://doi.org/10.1086/311269)
- Saxton, R. D., Read, A. M., Komossa, S., et al. 2017, *A&A*, 598, A29, doi: [10.1051/0004-6361/201629015](https://doi.org/10.1051/0004-6361/201629015)
- Sfaradi, I., Horesh, A., & Fender, R. 2022a, *Transient Name Server AstroNote*, 57, 1
- Sfaradi, I., Horesh, A., Fender, R., et al. 2022b, *ApJ*, 933, 176, doi: [10.3847/1538-4357/ac74bc](https://doi.org/10.3847/1538-4357/ac74bc)
- Sfaradi, I., Beniamini, P., Horesh, A., et al. 2024, *MNRAS*, 527, 7672, doi: [10.1093/mnras/stad3717](https://doi.org/10.1093/mnras/stad3717)
- Sfaradi, I., Chornock, R., Alexander, K. D., et al. 2025a, *Transient Name Server AstroNote*, 14, 1
- Sfaradi, I., Margutti, R., Chornock, R., et al. 2025b, *ApJL*, 992, L18, doi: [10.3847/2041-8213/ae0a26](https://doi.org/10.3847/2041-8213/ae0a26)
- Shen, R.-F., & Zhang, B. 2009, *MNRAS*, 398, 1936, doi: [10.1111/j.1365-2966.2009.15212.x](https://doi.org/10.1111/j.1365-2966.2009.15212.x)
- Short, P., Nicholl, M., Lawrence, A., et al. 2020, *MNRAS*, 498, 4119, doi: [10.1093/mnras/staa2065](https://doi.org/10.1093/mnras/staa2065)
- Sollerman, J., Fremling, C., Perley, D., & Laz, T. D. 2024, *Transient Name Server Discovery Report*, 2024-3166, 1
- Somalwar, J. J., Ravi, V., Yao, Y., et al. 2025, *ApJ*, 985, 175, doi: [10.3847/1538-4357/adcc19](https://doi.org/10.3847/1538-4357/adcc19)
- Stanek, K. Z. 2018, *Transient Name Server Discovery Report*, 2018-1325, 1
- . 2022, *Transient Name Server Discovery Report*, 2022-1433, 1
- Stein, R., van Velzen, S., Kowalski, M., et al. 2021, *Nature Astronomy*, 5, 510, doi: [10.1038/s41550-020-01295-8](https://doi.org/10.1038/s41550-020-01295-8)
- van Eerten, H. J., & Wijers, R. A. M. J. 2009, *MNRAS*, 394, 2164, doi: [10.1111/j.1365-2966.2009.14482.x](https://doi.org/10.1111/j.1365-2966.2009.14482.x)
- van Velzen, S., Gezari, S., Hung, T., et al. 2019a, *The Astronomer's Telegram*, 12568, 1
- van Velzen, S., Anderson, G. E., Stone, N. C., et al. 2016, *Science*, 351, 62, doi: [10.1126/science.aad1182](https://doi.org/10.1126/science.aad1182)
- van Velzen, S., Gezari, S., Cenko, S. B., et al. 2019b, *ApJ*, 872, 198, doi: [10.3847/1538-4357/aafe0c](https://doi.org/10.3847/1538-4357/aafe0c)
- van Velzen, S., Gezari, S., Hammerstein, E., et al. 2021, *ApJ*, 908, 4, doi: [10.3847/1538-4357/abc258](https://doi.org/10.3847/1538-4357/abc258)
- Velzen, S. v., Gezari, S., Cenko, S. B., et al. 2018, *The Astronomer's Telegram*, 12263, 1
- Wang, J.-Z., Lei, W.-H., Wang, D.-X., et al. 2014, *ApJ*, 788, 32, doi: [10.1088/0004-637X/788/1/32](https://doi.org/10.1088/0004-637X/788/1/32)
- Wang, Y., Baldi, R. D., del Palacio, S., et al. 2023, *MNRAS*, 520, 2417, doi: [10.1093/mnras/stad101](https://doi.org/10.1093/mnras/stad101)
- Wang, Y., Lin, Z., Wu, L., et al. 2025, *Science Advances*, 11, 25.9068, doi: [10.1126/sciadv.ady9068](https://doi.org/10.1126/sciadv.ady9068)
- Wevers, T., Pasham, D. R., van Velzen, S., et al. 2019, *MNRAS*, 488, 4816, doi: [10.1093/mnras/stz1976](https://doi.org/10.1093/mnras/stz1976)
- . 2021, *ApJ*, 912, 151, doi: [10.3847/1538-4357/abf5e2](https://doi.org/10.3847/1538-4357/abf5e2)
- Wevers, T., Coughlin, E. R., Pasham, D. R., et al. 2023, *ApJL*, 942, L33, doi: [10.3847/2041-8213/ac9f36](https://doi.org/10.3847/2041-8213/ac9f36)
- Yan, L., Wang, T., Jiang, N., et al. 2019, *ApJ*, 874, 44, doi: [10.3847/1538-4357/ab074b](https://doi.org/10.3847/1538-4357/ab074b)
- Yang, L., Shu, X., Mou, G., et al. 2025, *ApJL*, 993, L2, doi: [10.3847/2041-8213/ae0caa](https://doi.org/10.3847/2041-8213/ae0caa)

- Yao, Y., Chornock, R., LeBaron, N., et al. 2024, *Transient Name Server AstroNote*, 43, 1
- Yao, Y., Ravi, V., Gezari, S., et al. 2023, *ApJL*, 955, L6, doi: [10.3847/2041-8213/acf216](https://doi.org/10.3847/2041-8213/acf216)
- Yao, Y., Chornock, R., Ward, C., et al. 2025, *ApJL*, 985, L48, doi: [10.3847/2041-8213/add7de](https://doi.org/10.3847/2041-8213/add7de)
- Yuan, Q., Wang, Q. D., Lei, W.-H., Gao, H., & Zhang, B. 2016, *MNRAS*, 461, 3375, doi: [10.1093/mnras/stw1543](https://doi.org/10.1093/mnras/stw1543)
- Zauderer, B. A., Berger, E., Margutti, R., et al. 2013, *ApJ*, 767, 152, doi: [10.1088/0004-637X/767/2/152](https://doi.org/10.1088/0004-637X/767/2/152)
- Zhang, B. 2018, *The Physics of Gamma-Ray Bursts*, doi: [10.1017/9781139226530](https://doi.org/10.1017/9781139226530)
- Zhang, F., Shu, X., Yang, L., et al. 2024, *ApJL*, 962, L18, doi: [10.3847/2041-8213/ad1d61](https://doi.org/10.3847/2041-8213/ad1d61)
- Zhang, Z., Shu, X., Yang, L., et al. 2026, *ApJ*, 997, 9, doi: [10.3847/1538-4357/ae29f0](https://doi.org/10.3847/1538-4357/ae29f0)
- Zhou, C., Zhu, Z.-P., Lei, W.-H., et al. 2024, *ApJ*, 963, 66, doi: [10.3847/1538-4357/ad20f3](https://doi.org/10.3847/1538-4357/ad20f3)
- Zhuang, J., Shen, R.-F., Mou, G., & Lu, W. 2025, *ApJ*, 979, 109, doi: [10.3847/1538-4357/ad9b98](https://doi.org/10.3847/1538-4357/ad9b98)

APPENDIX

A. TDE WITH DETECTED RADIO EMISSION

Table A1. The informations of TDEs with radio detections.

Object	Redshift	Discovery band	Discovery time	Data reference
Swift J1644+57	0.354	γ ray	2011 March 25	Berger et al. (2012) Zauderer et al. (2013) Eftekhari et al. (2018) Cendes et al. (2021b)
Swift J1112-82	0.8901	γ ray	2011.06.16-19	Brown et al. (2017)
Swift J2058+05	1.1853	γ ray	2011.05.17-20	Cenko et al. (2012) Pasham et al. (2015) Brown et al. (2017)
AT2022cmc	1.19325	Optical	2022 February 11	Andreoni et al. (2022) Pasham et al. (2023) Rhodes et al. (2023)
EP250702a	1.036	X-ray	2025 July 2	Li et al. (2025) Levan et al. (2025)
Arp 299-B AT1	0.010411	Infrard	2005 January 30	Mattila et al. (2018)
ASASSN-14ae	0.0436	Optical	2014 January 25	Cendes et al. (2024c)
ASASSN-14li	0.0206	Optical	2014 November 22	Alexander et al. (2016) van Velzen et al. (2016) Bright et al. (2018) Anumarlapudi et al. (2024)
ASASSN-15oi	0.0484	Optical	2015 August 14	Horesh et al. (2021a) Hajela et al. (2025) Anumarlapudi et al. (2024)
AT2018bsi	0.051	Optical	2018 April 9	Cendes et al. (2024c)
AT2018cqh	0.048	Optical	2018 June 16	Zhang et al. (2024) Yang et al. (2025)
AT2018dyb/ASASSN-18pg	0.018	Optical	2018 July 11	Cendes et al. (2024c)
AT2018fyk/ASASSN-18ul	0.06	Optical	2018 September 8	Wevers et al. (2019) Wevers et al. (2021) Cendes et al. (2024b)
AT2018hco	0.088	Optical	2018 September 18	Horesh et al. (2018) Cendes et al. (2024c)
AT2018hyz/ASASSN-18zj	0.04573	Optical	2018 October 14	Gomez et al. (2020) Cendes et al. (2022) Sfaradi et al. (2024) Anumarlapudi et al. (2024) Cendes et al. (2024c)

Table A1. The radio TDEs samples (continued)

Object	The basic features (continued)			Radio data reference
	Redshift	Discovery band	First detected time	
				Cendes et al. (2025)
AT2018zr/PS18kh	0.071	Optical	2018 March 2	Cendes et al. (2024c)
AT2019ahk/ASASSN-19bt	0.0262	Optical	2019 January 29	Christy et al. (2024a) Anumarlapudi et al. (2024)
AT2019azh/ASASSN-19dj	0.022	Optical	2019 February 12	Goodwin et al. (2022) Sfaradi et al. (2022b) Anumarlapudi et al. (2024) Burn et al. (2025)
AT2019dsg	0.0512	Optical	2019 April 9	Stein et al. (2021) Cannizzaro et al. (2021) Cendes et al. (2021a) Mohan et al. (2022) Cendes et al. (2024c)
AT2019ehz	0.074	Optical	2019 April 29	Cendes et al. (2024c)
AT2019eve	0.081	Optical	2019 May 5	Cendes et al. (2024c)
AT2019qiz	0.01513	Optical	2019 September 18	O'Brien et al. (2019a) O'Brien et al. (2019b) Anumarlapudi et al. (2024) Alexander et al. (2025)
AT2019teq	0.0878	Optical	2019 October 20	Cendes et al. (2024c) this work
AT2020afhd	0.027	Optical	2024 January 1 ^a	Wang et al. (2025) Christy et al. (2024b)
AT2020mot	0.070	Optical	2020 June 14	Liodakis et al. (2023) Cendes et al. (2024c)
AT2020neh	0.062	Optical	2020 June 19	Cendes et al. (2024c)
AT2020nov	0.084	Optical	2020 June 27	Cendes et al. (2024c)
AT2020opy	0.159	Optical	2020 July 8	Goodwin et al. (2023a)
AT2020pj	0.068	Optical	2020 January 2	Cendes et al. (2024c)
AT2020vdq	0.045	Optical	2020 October 4	Somalwar et al. (2025) this work
AT2020vwl	0.0325	Optical	2020 October 08	Goodwin et al. (2023b) Goodwin et al. (2025b)
AT2020wey	0.027	Optical	2020 October 8	Cendes et al. (2024c)
AT2022dbl	0.0284	Optical	2022 February 22	Hinkle et al. (2024)
AT2022dsb	0.0235	X-ray	2022 February 17	Malyali et al. (2024) Anumarlapudi et al. (2024)
AT2024tvd	0.04494	Optical	2024 August 25	Sfaradi et al. (2025b)

Table A1. The radio TDEs samples (continued)

Object	The basic features (continued)			Radio data reference
	Redshift	Discovery band	First detected time	
CNSS J0019+00	0.018	Radio	2015 March 21	Anderson et al. (2020)
AT2020wjw/eRASSt J234403-352640	0.1	X-ray	2020 November 28	Goodwin et al. (2024)
AT2019avd/eRASSt J082337+042302	0.029/0.028	Optical	2019 February 9	Wang et al. (2023) Goodwin et al. (2025a)
eRASSt J011431-593654	0.16	X-ray	2020 November 24 ^b	Goodwin et al. (2025a)
eRASSt J142140-295321	0.056	X-ray	2020 January 30 ^b	Goodwin et al. (2025a)
eRASSt J143624-174105	$0.19^{+0.06}_{-0.03}$	X-ray	2022 February 18 ^b	Goodwin et al. (2025a)
eRASSt J210858-562832	0.043	X-ray	2020 October 26 ^b	Goodwin et al. (2025a)
FIRST J153350.8+272729	0.03243	Radio	1986 November 6–December 13	Ravi et al. (2022)
IGR J12580+0134	0.00411	X-ray	2011 January 6	Irwin et al. (2015)
				Yuan et al. (2016)
				Perlman et al. (2017)
				Perlman et al. (2022)
iPTF 16fnl	0.016328	Optical	2016 August 26	Horesh et al. (2021b) Cendes et al. (2024c)
OGLE17aaj	0.116	Optical	2017 January 2	Cendes et al. (2024c)
PS16dtm / SN2016ezh	0.0804	Optical	2016 August 12	Cendes et al. (2024c)
SDSS J1115+0544	0.08995	Infrared	2015 May 28 ^c	Zhang et al. (2026)
Swift J0230+28	0.036	X-ray	2022 June 22	Guolo et al. (2024)
WTP14adeqka	0.01895	Infrared	2015 June 20	Golay et al. (2025)
XMMSL1 J0740-85	0.0173	X-ray	2014 April 1	Alexander et al. (2017)
eRASSt J045650.3-203750	0.077	X-ray	2020 September 8	Liu et al. (2024)
AT2019aalc	0.0356	Optical	2019 January 22	Milán Veres et al. (2024) ^d

^a The initial date of the optical rebrightening (Wang et al. 2025).

^b The time of the peak eROSITA X-ray flux measurement.

^c The time of optical peak.

^d The radio data have not been released.

In this work, we incorporate additional archival VLA observations of AT2019teq and AT2020vdq obtained from the NRAO Science Data Archive. For AT2019teq, we use observations from programs 24A-322 (PI: Cendes), 20B-377 (PI: Alexander), and 23A-241 (PI: Cendes), together with data products from VLASS 4.1. For AT2020vdq, we analyze VLA observations from programs 23A-409 (PI: Somalwar) and 21B-322 (PI: Hallinan), as well as data products from VLASS 3.2. The data reduction was carried out using the Common Astronomy Software Applications package (CASA 6.5.4), following standard VLA calibration procedures. The visibility data were calibrated using the automated VLA calibration pipeline provided in CASA. Primary flux density and bandpass calibration were performed using standard calibrators (3C147 or 3C286), depending on the observing epoch, while nearby phase calibrators were used for gain calibration. After pipeline processing, the data were manually inspected and additional flagging was applied to remove radio frequency interference (RFI) and poorly calibrated scans when necessary. Imaging was performed using the CASA task TCLEAN in multi-scale multi-frequency synthesis (MS-MFS) mode to properly account for the wide fractional bandwidth and possible spectral variations. We adopted Briggs weighting with a robust parameter of 0 or 2 to achieve an optimal compromise between angular resolution and sensitivity. The flux density of AT2019teq and

AT2020vdq was measured by fitting a point-source Gaussian model in the image plane using the CASA task IMFIT. The local image rms noise was estimated with IMSTAT in nearby source-free regions. The flux density uncertainty was calculated as the quadratic sum of the image rms, the IMFIT fitting uncertainty, and a typical systematic calibration uncertainty of 5%. All measured flux densities and upper limits are summarized in Table [A2](#).

Table A2. Radio observations of AT2019teq and AT2020vdq.

Object	Telescope	Project Code / Source	Date of Observation	δt (d)	Frequency (GHz)	Flux Density (mJy)
AT2019teq	VLA	20B-377	2022 Nov 26	1133	5.0	0.26 ± 0.021
—	—	—	—	—	6.0	0.217 ± 0.015
—	—	—	—	—	7.0	0.171 ± 0.013
—	—	—	—	—	9.0	0.16 ± 0.014
—	—	—	—	—	11.0	0.118 ± 0.013
—	—	23A-241	2023 Sep 12	1423	1.5	0.311 ± 0.029
—	—	—	—	—	3.0	0.203 ± 0.021
—	—	—	—	—	5.0	0.138 ± 0.019
—	—	—	—	—	6.0	0.115 ± 0.011
—	—	—	—	—	7.0	0.097 ± 0.019
—	—	—	—	—	9.0	< 0.08
—	—	—	—	—	11.0	< 0.08
—	—	24A-322	2024 Sep 11	1788	6.0	0.141 ± 0.01
—	—	VCLASS 4.1	2025 Sep 23	2165	3.0	< 0.371
AT2020vdq	—	VCLASS 3.2	2024 Jul 9	1374	3.0	< 0.381
—	—	21B-322	2022 Feb 2	486	1.5	0.953 ± 0.09
—	—	—	—	—	3.0	1.485 ± 0.09
—	—	—	—	—	3.5	1.717 ± 0.11
—	—	—	—	—	4.5	1.906 ± 0.11
—	—	—	—	—	5.0	1.897 ± 0.10
—	—	—	—	—	5.5	1.833 ± 0.12
—	—	—	—	—	6.5	1.656 ± 0.12
—	—	—	—	—	7.5	1.535 ± 0.12
—	—	—	—	—	8.5	1.370 ± 0.11
—	—	—	—	—	9.0	1.259 ± 0.08
—	—	—	—	—	9.5	1.100 ± 0.07
—	—	—	—	—	10.5	1.006 ± 0.08
—	—	—	—	—	11.0	0.884 ± 0.06
—	—	—	—	—	11.5	0.825 ± 0.06
—	—	23A-409	2023 May 26	964	2.5	0.737 ± 0.05
—	—	—	—	—	3.0	0.611 ± 0.04
—	—	—	—	—	3.5	0.510 ± 0.04
—	—	—	—	—	4.5	0.427 ± 0.03
—	—	—	—	—	5.0	0.441 ± 0.03
—	—	—	—	—	5.5	0.359 ± 0.02
—	—	—	—	—	6.5	0.297 ± 0.03
—	—	—	—	—	7.5	0.247 ± 0.03
—	—	—	—	—	8.5	0.146 ± 0.02
—	—	—	—	—	9.5	0.192 ± 0.02
—	—	—	—	—	10.5	0.181 ± 0.02
—	—	—	—	—	11.5	0.147 ± 0.02
—	—	—	—	—	22.5	0.097 ± 0.01

NOTE— δt is measured relative to the first detection date.